MOX–Report No. 51/2014

A priori anisotropic mesh adaptation on implicitly defined surfaces

Dassi, F.; Perotto, S.; Formaggia, L.

MOX, Dipartimento di Matematica "F. Brioschi"
Politecnico di Milano, Via Bonardi 9 - 20133 Milano (Italy)

mox@mate.polimi.it http://mox.polimi.it

A priori anisotropic mesh adaptation on implicitly defined surfaces

Franco Dassi*, Simona Perotto and Luca Formaggia♯

November 10, 2014

♯ MOX– Modellistica e Calcolo Scientifico
Dipartimento di Matematica, Politecnico di Milano
Piazza Leonardo da Vinci 32, 20133 Milano, Italy
{franco.dassi,simona.perotto,luca.formaggia}@polimi.it

Keywords: anisotropic error estimates, interpolation error, metric-based mesh adaptation, finite elements on surfaces

AMS Subject Classification: 65D05, 65N15, 65N50, 65N30

Abstract

Mesh adaptation on surfaces demands particular care due to the important role played by the fitting of the surface. We propose an adaptive procedure based on a new error analysis which combines a rigorous anisotropic estimator for the L^1-norm of the interpolation error with an anisotropic and more heuristic control of the geometric error. We resort to a metric-based adaptive algorithm which employs local operations to modify the initial mesh according to the information provided by the error analysis. An extensive numerical validation corroborates the robustness of the error analysis as well as of the adaptive procedure.

1 Introduction and motivations

Mesh adaptation on surfaces is a topic of great interest in the scientific panorama due to its potential strong impact with a view to practical applications (see, e.g., [41, 45] among the most recent papers) and, more in general, to the approximation of partial differential equations on manifolds. Despite the relevance of this research field, there exists still a limited number of works dealing with surface mesh adaptive techniques based on a rigorous error analysis, and it turns out to be essentially confined to an isotropic context [2, 14, 17, 33, 39].

*Current affiliation:Weierstrass Institute for Applied Analysis and Stochastics, Berlin.

In this paper we focus on implicitly defined surfaces $\Gamma \subset \mathbb{R}^3$ and we derive an anisotropic *a-priori* error estimator to control the error associated with the approximation of a generic function $f \in H^1(\Gamma)$ via a piecewise linear quasi-interpolant operator. The triangular surface grid used to define the interpolant is also employed to approximate surface Γ. This choice leads us to include in the error analysis a contribution due to the geometric approximation in addition to the interpolation error term. In this respect, we are consistent with the decomposition of the error provided in [14] in terms of a contribution related to the finite element approximation of f, a term associated with the geometric approximation of Γ and a contribution taking into account data approximation. In particular, since we deal with an interpolation error analysis, we are allowed to neglect the data error while we identify the discretization with the interpolation error.

The interest for an anisotropic setting is mainly justified by the several possible applicative fields of interest in Scientific Computing (e.g., in a biomedical, geological or aerodynamic context), where phenomena may exhibit large variations along a certain direction with less significant changes along the other ones. In such cases, a standard isotropic adaptive algorithm may generate a very large number of elements to ensure a certain accuracy or, vice versa, may provide a limited accuracy for a fixed number of elements. This is a well-established issue in the standard planar case (see, e.g., [6, 7, 37, 42, 47]) and it is expected to work analogously on surfaces, where the directionalities of the domain may be taken into account as well, via a proper sizing, shaping and orientation of the mesh elements.

The idea pursued in this work is to properly merge the interpolation analysis developed in [14] with the anisotropic setting proposed in [22] for a 2D planar setting, and then successfully extended to a 3D volumetric framework in [19, 20]. In particular, the derivation of an anisotropic counterpart for the Poincaré inequality represents the crucial result with a view to the desired anisotropic control of the interpolation error. Concerning the anisotropic bound for the geometric error, we move essentially from heuristic considerations, numerically checked in the last section of the paper.

The information provided by the global (interpolation plus geometric) error estimator is successively converted into a practical procedure to adapt the mesh. For this purpose, we resort to a metric-based approach with the aim of reducing the number of mesh elements to guarantee a certain accuracy on the solution while equidistributing the error. To combine the interpolation with the geometric information, we propose different strategies and we compare them in the last section of the paper to identify, possibly, the most suited approach with a view to an anisotropic mesh adaptivity. We use standard local mesh operations (edge swapping, splitting and collapsing, and node smoothing) to change the initial (isotropic) mesh into the final adapted mesh matching the directional features of the function and of the surface at hand. The employment of local operations is a novelty in the context of the anisotropic approach proposed in [22, 23], where a metric-based remeshing of the initial grid is essentially performed.

Finally, we remark that the proposed approach based on an implicit representa-

tion of the surface relieves us from too specific requirements on possible surfaces of interest as done, for instance, in [2, 39].

The paper is organized as follows. In § 2 we settle the reference geometric setting and we introduce the basic ideas of the anisotropic framework. Section 3 represents the theoretical core of the paper since it collects the derivation of the anisotropic estimator for the interpolation error and the proposal of the anisotropic control for the geometric error. In § 4 we tackle the crucial issue of merging the interpolation analysis with the geometric information by exploring different possibilites. Section 5 provides an exhaustive numerical investigation, first by setting the adaptive procedure and then by validating it on both a closed and an open surface. The last section is meant to draw some conclusions starting from the numerical assessment.

2 The geometric setting

Let us consider a connected C^2-compact and orientable two-dimensional surface Γ embedded in $\mathbb{R}^3$. In particular, we adopt an implicit representation for Γ, i.e., we assume that Γ coincides with the zero level set of a signed distance function $d : U_0 \subset \mathbb{R}^3 \to \mathbb{R}$, such that $d(\mathbf{x}) = \mathrm{dist}(\mathbf{x}, \Gamma)$ for any $\mathbf{x} = (x_1, x_2, x_3)' \in U_0$, and with U_0 an open subset of $\mathbb{R}^3$. In particular, if Γ is a closed surface, we assume $d < 0$ inside the volume enclosed by Γ whereas $d > 0$ outside, while, if Γ is an open surface, we assume $\partial\Gamma$ to be piecewise curvilinear in a sense that will be specified below.

Now, following [14], we assume that there exists a *shell* of width $\delta > 0$ around Γ given by $U_\delta = \{\mathbf{x} \in \mathbb{R}^3 : |\mathrm{dist}(\mathbf{x})| < \delta\} \subset U_0$ (see Figure 1). In particular, the thickness δ of the shell is sufficiently small to guarantee the global uniqueness of the decomposition

$$\mathbf{x} = a(\mathbf{x}) + d(\mathbf{x})\mathbf{n}(\mathbf{x}) \quad \forall \mathbf{x} \in U_\delta, \tag{1}$$

with $a : U_\delta \to \Gamma$ the orthogonal projection operator onto Γ and $\mathbf{n}(\mathbf{x}) = \nabla d(\mathbf{x})$ the outward unit normal to Γ at $\mathbf{x}$. More details about the choice of δ can be found, e.g., in [14, 29]. The projection a is instrumental in extending the definition of a function f assigned on Γ to the whole shell U_δ, thanks to the following relation

$$f^E(\mathbf{x}) = f(a(\mathbf{x})) \quad \forall \mathbf{x} \in U_\delta. \tag{2}$$

Essentially, the extended function f^E can be identified with the extension along wires of the function f (see Figure 1). Via f^E, we may define the tangential gradient $\nabla_\Gamma f$ on Γ of the function $f : \Gamma \to \mathbb{R}$ as

$$\nabla_\Gamma f = \nabla f^E - (\mathbf{n} \cdot \nabla f^E)\mathbf{n}, \tag{3}$$

with ∇ the standard gradient operator in $\mathbb{R}^3$. Notice that, thanks to (2), the tangential gradient $\nabla_\Gamma f$ depends only on the values of f on Γ despite definition (3) involves the whole shell U_δ.

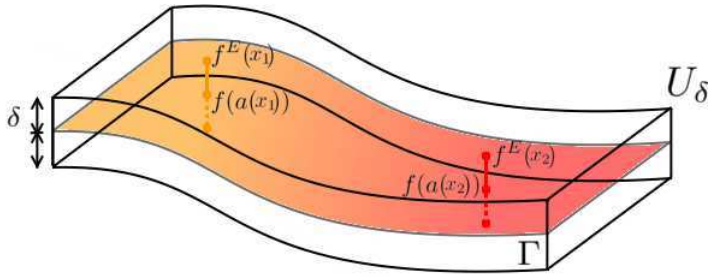

Figure 1: Schematic representation of the shell U_δ and of the extended function f^E in (2).

Now, in view of practical computations, we replace surface Γ with a polyhedral surface $\Gamma_h \subset U_\delta$ consisting of a set $\mathcal{T}_h = \{T\}$ of triangular faces T of diameter h_T, such that $\Gamma_h \equiv \cup_{T\in\mathcal{T}_h} T$. We denote by $\mathcal{V}$ the set of the vertices of Γ_h and we demand $\mathcal{V} \subset \Gamma$. Let $\mathbf{n}_h$ be the piecewise constant unit outer normal to Γ_h. We assume $\mathbf{n} \cdot \mathbf{n}_h > 0$ everywhere on Γ_h. Moreover, since $\Gamma_h \subset U_\delta$, we can employ the orthogonal projection defined in (1) to relate Γ_h with Γ as well, by demanding $a : \Gamma_h \to \Gamma$ to be bijective. The Jacobian associated with such a bijection is denoted by μ_h, i.e., we have that

$$\mu_h(\mathbf{x}) d\Gamma_h(\mathbf{x}) = d\Gamma(a(\mathbf{x})) \quad \forall \mathbf{x} \in \Gamma_h. \tag{4}$$

Finally, if Γ is an open surface, we require $\partial\Gamma \equiv a(\partial\Gamma_h)$. This implies to assume $\partial\Gamma$ piecewise linear, i.e., we are completely relieved from any error due to the approximation of the boundary of Γ.

Analogously, any function f is replaced by a discrete counterpart f_h. For this purpose, we introduce the space X_h of the continuous functions which are affine on each face T of Γ_h [17] and we approximate f with a function $f_h \in X_h$ to be properly defined. We denote by $\varphi_{\mathbf{z}_i} \in X_h$ the standard basis function associated with the vertex $\mathbf{z}_i \in \mathcal{V}$, such that $\varphi_{\mathbf{z}_i}(\mathbf{z}_j) = \delta_{ij}$, for any $\mathbf{z}_i, \mathbf{z}_j \in \mathcal{V}$, with δ_{ij} the Kronecker symbol.

An anisotropic estimate for the difference between f and f_h will drive the adaptive procedure presented in the next sections. In particular, f_h will be identified with an interpolant of f.

2.1 Source of the anisotropic information

To deal with anisotropic grids, we need more information about the mesh elements with respect to the isotropic case. Indeed, the goal is to uniquely define not only the size, according to an isotropic approach, but also the shape and the orientation of each face T of the mesh. For this purpose, we extend the approach proposed in [22] for a 2D planar setting to a non-planar framework.

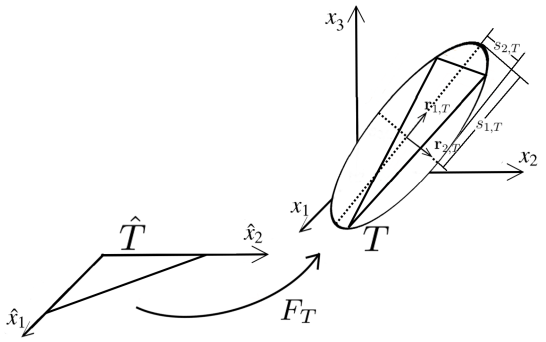

Figure 2: Geometric interpretation of the map F_T and of the main anisotropic quantities.

We choose as source for the anisotropic information the invertible affine map F_T from a reference planar triangle $\widehat{T} \subset \mathbb{R}^2$ to the general (non degenerate) triangle $T \in \mathcal{T}_h$ embedded in $\mathbb{R}^3$ (see Figure 2). The map $F_T : \widehat{T} \to T$ is defined by

$$\mathbf{x} = (x_1, x_2, x_3)' = F_T(\widehat{\mathbf{x}}) = M_T \widehat{\mathbf{x}} + \mathbf{b}_T \in T, \tag{5}$$

with $\widehat{\mathbf{x}} = (\widehat{x}_1, \widehat{x}_2)' \in \widehat{T}$, $M_T \in \mathbb{R}^{3\times 2}$ and $\mathbf{b}_T \in \mathbb{R}^3$. In particular, we select as reference element $\widehat{T}$ the triangle with vertices $(0,0)$, $(1,0)$, $(0,1)$, i.e., the unit right triangle. For this choice, we have

$$M_T = \begin{bmatrix} v_1^2 - v_1^1 & v_1^3 - v_1^1 \\ v_2^2 - v_2^1 & v_2^3 - v_2^1 \\ v_3^2 - v_3^1 & v_3^3 - v_3^1 \end{bmatrix}, \quad \mathbf{b}_T = \begin{bmatrix} v_1^1 \\ v_2^1 \\ v_3^1 \end{bmatrix},$$

where $\mathbf{v}^j = (v_1^j, v_2^j, v_3^j)'$, for $j = 1, 2, 3$, denotes the j-th vertex of the triangle T.

The anisotropic information of each triangle T is derived moving from the spectral properties of the matrix M_T. In particular, we resort to the singular value decomposition (SVD) of M_T given by $M_T = U_T \Sigma_T V_T'$, where $U_T \in \mathbb{R}^{3\times 3}$ and $V_T \in \mathbb{R}^{2\times 2}$ are unitary matrices, while $\Sigma_T = \mathrm{diag}(\mathrm{s_{1,T}}, \mathrm{s_{2,T}}) \in \mathbb{R}^{3\times 2}$ is a rectangular diagonal matrix with non-negative real entries representing the singular values of M_T [31]. The columns of the matrices $U_T = [\mathbf{r}_{1,T}, \mathbf{r}_{2,T}, \mathbf{n}_h]$ and V_T collect the left- and right-singular vectors of M_T, respectively. The SVD of M_T allows us to completely characterize the triangle $T \in \mathcal{T}_h$. In particular, the singular values of M_T measure the lengths of the semi-axes of the ellipse circumscribing T and lying on the plane identified by T, while the singular vectors $\mathbf{r}_{1,T}$ and $\mathbf{r}_{2,T}$ provide the directions of these semi-axes (see Figure 2). Without loss of generality, henceforth we assume $s_{1,T} \geq s_{2,T}$. Moreover, we introduce the definition of *aspect ratio* $\sigma_T = s_{1,T}/s_{2,T}$, which quantifies the deformation of the element T. In particular, the aspect ratio is always greater than or equal to one, with $\sigma_T = 1$

when T coincides with an equilateral triangular face. Notice that the vector $\mathbf{b}_T$ in (5) is simply associated with a shift and does not play any role in identifying the shape of T.

Now, in view of a mesh adaptation procedure, we define a suitable interpolation operator. Here and throughout the paper, we adopt a standard notation for both the Lebesgue and Sobolev spaces of functions defined on surfaces as well as for the associated norms (see, e.g., [16, 17]). Following [14], given a function $f : \Gamma \to \mathbb{R}$ such that $f \in L^1(\Gamma)$, we first introduce the averaged nodal values

$$f^E_{\mathbf{z}} = \frac{1}{\int_{\omega_{\mathbf{z}}} \varphi_{\mathbf{z}}\, d\omega_{\mathbf{z}}} \int_{\omega_{\mathbf{z}}} \varphi_{\mathbf{z}} f^E\, d\omega_{\mathbf{z}} \quad \forall \mathbf{z} \in \mathcal{V}, \tag{6}$$

where $\omega_{\mathbf{z}}$ is the patch of the faces in Γ_h sharing vertex $\mathbf{z}$, f^E is the extension of the function f to U_δ according to (2) and $\varphi_{\mathbf{z}}$ is the basis function associated with vertex $\mathbf{z}$. Thus, the interpolant we are interested in is given by

$$I_h f^E(\mathbf{x}) = \sum_{\mathbf{z}\in\mathcal{V}} f^E_{\mathbf{z}} \varphi_{\mathbf{z}}(\mathbf{x}) \quad \forall f \in L^1(\Gamma). \tag{7}$$

Actually, I_h is a quasi-interpolant operator, similarly to the well-known Clément or Scott-Zhang interpolants ([9, 46]; see, e.g., also [2, 21, 22]). Moreover, we remark that, since functions $\{\varphi_{\mathbf{z}}\}_{\mathbf{z}\in\mathcal{V}}$ constitute a partition of unity, the $L^1(\Gamma_h)$-norm of the interpolation error is identically equal to zero, i.e., we have

$$\int_{\Gamma_h} \left(f^E - I_h f^E\right) d\Gamma_h = \sum_{\mathbf{z}\in\mathcal{V}} \int_{\omega_{\mathbf{z}}} \left(f^E - f^E_{\mathbf{z}}\right)\varphi_{\mathbf{z}}\, d\omega_{\mathbf{z}} = 0,$$

being $\mathrm{supp}(\varphi_{\mathbf{z}}) = \omega_{\mathbf{z}}$. In the sequel, we identify the approximation $f_h \in X_h$ for the generic function f defined on Γ with the interpolant in (7). In particular, an anisotropic control for the $L^1(\Gamma)$-norm of the error $f - f_h$ (i.e., $f - I_h f^E$) will drive the mesh adaptive procedure presented in this paper.

3 Anisotropic error estimates

The results in this section provide the theoretical tool at the basis of the proposed adaptive procedure. We exploit the standard decomposition of the error into a contribution related to the finite element approximation and a contribution associated with the geometric approximation of the surface Γ via Γ_h [14]. In particular, since we deal with an interpolation error analysis, we neglect any error associated with the data approximation, as well as we identify the discretization with the interpolation error. The idea pursued in the following is to provide an anisotropic control for both the interpolation and the geometric errors.

3.1 The interpolation error

To derive an anisotropic bound for the interpolation error $f - I_h f^E$ associated with the operator (7), we preliminarly prove the following result which generalizes Lemma 2.2 in [14] to an anisotropic context.

Lemma 1 (anisotropic Poincaré inequality) *Let $f \in H^1(\Gamma)$. Then, for each node $\mathbf{z} \in \mathcal{V}$, there exists a constant C such that*

$$||f^E - f^E_{\mathbf{z}}||_{L^2(\omega_{\mathbf{z}})} \leq C\Big[\sum_{T\in\omega_{\mathbf{z}}}\Big(\sum_{i=1}^{2} s^2_{i,T}\,\mathbf{r}'_{i,T} G_T(f^E)\mathbf{r}_{i,T}\Big)\Big]^{1/2}, \tag{8}$$

with $f^E : U_\delta \to \mathbb{R}$ the extension of f to U_δ according to (2)*, $f^E_{\mathbf{z}}$ defined as in* (6)*, and where G_T is the symmetric positive semi-definite matrix given by*

$$G_T(f^E) = \begin{bmatrix} \displaystyle\int_T (g_1)^2\,dT & \displaystyle\int_T g_1 g_2\,dT & \displaystyle\int_T g_1 g_3\,dT \\ \displaystyle\int_T g_1 g_2\,dT & \displaystyle\int_T (g_2)^2\,dT & \displaystyle\int_T g_2 g_3\,dT \\ \displaystyle\int_T g_1 g_3\,dT & \displaystyle\int_T g_2 g_3\,dT & \displaystyle\int_T (g_3)^2\,dT \end{bmatrix}, \tag{9}$$

where $g_i = \left(\nabla_{\Gamma_h} f^E\right)_i$, for $i = 1, 2, 3$, denotes the i-th component of the tangential gradient $\nabla_{\Gamma_h} f^E = \nabla f^E - (\mathbf{n}_h \cdot \nabla f^E)\mathbf{n}_h$ with respect to the standard Cartesian coordinate system in $\mathbb{R}^3$.

Proof The first part of this proof exactly follows proof of Lemma 2.2 in [14]. Thanks to definition (6) and the Cauchy-Schwarz inequality, we first get

$$||f^E_{\mathbf{z}}||_{L^2(\omega_{\mathbf{z}})} = |\omega_{\mathbf{z}}|^{1/2}|f^E_{\mathbf{z}}| \leq |\omega_{\mathbf{z}}|^{1/2}\frac{||\varphi_{\mathbf{z}}||_{L^2(\omega_{\mathbf{z}})}}{||\varphi_{\mathbf{z}}||_{L^1(\omega_{\mathbf{z}})}}||f^E||_{L^2(\omega_{\mathbf{z}})}, \tag{10}$$

with $|\varpi|$ the measure of a generic set $\varpi \subset \mathbb{R}^d$, for $d = 1, 2, 3$. Now, by exploiting the map F_T in (5), for each $T \in \omega_{\mathbf{z}}$, we consider the piecewise affine map $F_{\mathbf{z}} : \widehat{\omega}_{\mathbf{z}} \to \omega_{\mathbf{z}}$, where $\widehat{\omega}_{\mathbf{z}}$ coincides with the union of the inverse image $F_T^{-1}(T)$ of all the triangles T constituting the patch $\omega_{\mathbf{z}}$. Analogoulsly, we denote by $\widehat{u}$ the inverse image of a generic function $u \in H^1(\Gamma_h)$ via the map F_T. The $L^2(\omega_{\mathbf{z}})$- and the $L^1(\omega_{\mathbf{z}})$-norms in (10) can be easily computed coming back to the reference framework as

$$\|\varphi_{\mathbf{z}}\|^p_{L^p(\omega_{\mathbf{z}})} = \sum_{T\in\omega_{\mathbf{z}}}\int_T (\varphi_{\mathbf{z}})^p\,dT = \sum_{T\in\omega_{\mathbf{z}}}\frac{|T|}{|\widehat{T}|}\int_{\widehat{T}}(\widehat{\varphi}_{\mathbf{z}})^p\,d\widehat{T} = |\omega_{\mathbf{z}}|\,\frac{\int_{\widehat{T}}(\widehat{\varphi}_{\mathbf{z}})^p\,d\widehat{T}}{|\widehat{T}|}, \tag{11}$$

where $\|\widehat{\varphi}_{\mathbf{z}}\|_{L^1(\widehat{T})} = 1/6$, $\|\widehat{\varphi}_{\mathbf{z}}\|_{L^2(\widehat{T})} = 1/\sqrt{12}$, and $|\widehat{T}| = 1/2$. By substituting (11) in (10), we get

$$||f^E_{\mathbf{z}}||_{L^2(\omega_{\mathbf{z}})} \leq \sqrt{\frac{3}{2}}\,||f^E||_{L^2(\omega_{\mathbf{z}})}.$$

In a similar way, for a constant $K \in \mathbb{R}$ and thanks to definition (6) and to the Cauchy-Schwarz inequality, we have

$$\|f^E_{\mathbf{z}} - K\|_{L^2(\omega_{\mathbf{z}})} = |\omega_{\mathbf{z}}|^{1/2} |f^E_{\mathbf{z}} - K| = \frac{|\omega_{\mathbf{z}}|^{1/2}}{\left| \int_{\omega_{\mathbf{z}}} \varphi_{\mathbf{z}} \, d\omega_{\mathbf{z}} \right|} \left| \int_{\omega_{\mathbf{z}}} (f^E - K) \varphi_{\mathbf{z}} \, d\omega_{\mathbf{z}} \right|$$

$$\leq \frac{|\omega_{\mathbf{z}}|^{1/2}}{\|\varphi_{\mathbf{z}}\|_{L^1(\omega_{\mathbf{z}})}} \|f^E - K\|_{L^2(\omega_{\mathbf{z}})} \|\varphi_{\mathbf{z}}\|_{L^2(\omega_{\mathbf{z}})} \leq \sqrt{\frac{3}{2}} \|f^E - K\|_{L^2(\omega_{\mathbf{z}})}.$$

The triangle inequality immediately yields

$$||f^E - f^E_{\mathbf{z}}||_{L^2(\omega_{\mathbf{z}})} \leq \left(1 + \sqrt{\frac{3}{2}}\right) ||f^E - K||_{L^2(\omega_{\mathbf{z}})}. \tag{12}$$

Now, the idea is to properly select the constant K and to exploit the spectral decomposition introduced for M_T to obtain an anisotropic bound for the right-hand side in (12). We choose $K = |\widehat{T}|^{-1} \displaystyle\int_{\widehat{T}} \eta(\widehat{\mathbf{x}}) \, d\widehat{T}$, where η is a function defined on $\widehat{T}$ such that $\eta(\widehat{\mathbf{x}}) = f^E(F_T(\widehat{\mathbf{x}}))$, for any $\widehat{\mathbf{x}} \in \widehat{T}$. Thus, thanks to the standard Poincaré inequality, we have

$$\|f^E - f^E_{\mathbf{z}}\|^2_{L^2(\omega_{\mathbf{z}})} \leq C \sum_{T \in \omega_{\mathbf{z}}} \frac{|T|}{|\widehat{T}|} \int_{\widehat{T}} \left(\eta - K\right)^2 d\widehat{T} \leq C \sum_{T \in \omega_{\mathbf{z}}} \frac{|T|}{|\widehat{T}|} \int_{\widehat{T}} \left(\widehat{\nabla}\eta\right)^2 d\widehat{T},$$

with $\widehat{\nabla}$ the gradient operator associated with the coordinate system $(\widehat{x}_1, \widehat{x}_2)$ in the reference setting, and where C does include the constant value in (12) and the Poincaré constant as well. We remark that $\widehat{\nabla}\eta = M_T' \nabla_{\Gamma_h} f^E$. This yields, coming back to Γ_h, that

$$\|f^E - f^E_{\mathbf{z}}\|^2_{L^2(\omega_{\mathbf{z}})} \leq C \sum_{T \in \omega_{\mathbf{z}}} \int_T \left| M_T' \nabla_{\Gamma_h} f^E \right|^2 dT.$$

To introduce the anisotropic information, we resort to the SVD of $M_T = U_T \Sigma_T V_T'$, to have

$$\|f^E - f^E_{\mathbf{z}}\|^2_{L^2(\omega_{\mathbf{z}})} \leq C \sum_{T \in \omega_{\mathbf{z}}} \int_T \left[\left(\nabla_{\Gamma_h} f^E\right)' U_T \Sigma_T \Sigma_T' U_T' \left(\nabla_{\Gamma_h} f^E\right) \right] dT, \tag{13}$$

where matrix V_T does not provide any contribution since $V_T' V_T = I$. Now, the product $U_T \Sigma_T \Sigma_T' U_T'$ in (13) can be easily expressed in terms of the anisotropic lengths $s_{i,T}$ and directions $\mathbf{r}_{i,T}$ as

$$U_T \Sigma_T \Sigma_T' U_T' = \sum_{i=1}^{2} s^2_{i,T} \, \mathbf{r}_{i,T} \otimes \mathbf{r}_{i,T},$$

$\otimes$ denoting the standard outer product between vectors. This leads to rewrite (13) as

$$\|f^E - f^E_{\mathbf{z}}\|^2_{L^2(\omega_{\mathbf{z}})} \leq C \sum_{T\in\omega_{\mathbf{z}}} \Big[\sum_{i=1}^{2} s^2_{i,T} \int_T \big(\nabla_{\Gamma_h} f^E\big)' \mathbf{r}_{i,T} \otimes \mathbf{r}_{i,T} \big(\nabla_{\Gamma_h} f^E\big)\, dT \Big].$$

Straightforward algebraic manipulations show that

$$\big(\nabla_{\Gamma_h} f^E\big)' \mathbf{r}_{i,T} \otimes \mathbf{r}_{i,T} \big(\nabla_{\Gamma_h} f^E\big) = \mathbf{r}'_{i,T} \nabla_{\Gamma_h} f^E \otimes \nabla_{\Gamma_h} f^E \mathbf{r}_{i,T} = \mathbf{r}'_{i,T} G_T(f^E) \mathbf{r}_{i,T},$$

with G_T defined as in (9). This completes the proof.

□

Remark 3.1 *The quantity C in* (8) *actually coincides with a constant value since it does not depend on any geometric feature nor on the regularity of the function f. Moreover, the introduction of the shell U_δ containing the surface of interest allows us to manage the tangential gradient as a standard three-dimensional entity. This device justifies that the matrix in* (9) *has a rank at most equal to two.*

As expected, the anisotropic estimate (8) provides as a particular case the corresponding isotropic estimate, i.e., inequality (2.2.29) in [14]. Estimate (8) exhibits a more complex structure with respect to the isotropic result but it provides more information about the element T. In particular, the diameter $h_{\mathbf{z}}$ of the patch characterizing the isotropic estimate is replaced in (8) by the anisotropic lengths $s_{i,T}$, with $i = 1, 2$. Likewise, the first order derivatives involved in the $L^2(\omega_{\mathbf{z}})$-norm of $\nabla_{\Gamma_h} f^E$ in the isotropic case are now projected along the anisotropic directions $\mathbf{r}_{i,T}$, with $i = 1, 2$, via the products $\mathbf{r}'_{i,T} G_T(f^E) \mathbf{r}_{i,T}$. This richness of information will allow us to fix, in a predictive way, the *size* (usually tuned by the diameter) together with the *shape* and the *orientation* of the generic element $T \in \mathcal{T}_h$ by setting the quantities $s_{i,T}$ and $\mathbf{r}_{i,T}$, respectively. The intrinsic potentiality of estimate (8) becomes more evident by rewriting it in terms of the aspect ratio σ_T as

$$\|f^E - f^E_{\mathbf{z}}\|_{L^2(\omega_{\mathbf{z}})} \leq C \Big[\sum_{T\in\omega_{\mathbf{z}}} |T| \Big(\sigma_T \mathbf{r}'_{1,T} G_T(f^E) \mathbf{r}_{1,T} + \frac{1}{\sigma_T} \mathbf{r}'_{2,T} G_T(f^E) \mathbf{r}_{2,T} \Big) \Big]^{1/2}, \tag{14}$$

where we have exploited the relation $|T| = |\widehat{T}| s_{1,T} s_{2,T}$ by including the constant area $|\widehat{T}| = 1/2$ into C. Thus, $|T|$ provides the information associated with the size of T, the shape of T is identified by the aspect ratio σ_T, whereas the orientation of T is fixed by the directions $\mathbf{r}_{1,T}$ and $\mathbf{r}_{2,T}$.

Next result represents the main theoretical statement of this paper and it will play a crucial role in setting the anisotropic mesh adaptive procedure.

Proposition 2 *Let $f \in H^1(\Gamma)$ and let $f^E : U_\delta \to \mathbb{R}$ be the extension of f to U_δ according to* (2)*. Then, there exists a constant C such that*

$$\|f - I_h f^E\|_{L^1(\Gamma)} \leq C \sum_{T\in\mathcal{T}_h} |T|^{1/2} \alpha_T \nu_T(\sigma_T, \mathbf{r}_{1,T}, f^E), \tag{15}$$

where $\alpha_T = \sum_{\mathbf{z}\in T} \|\varphi_{\mathbf{z}}\mu_h\|_{L^2(\omega_{\mathbf{z}})}$*, with* μ_h *defined as in* (4) *and* $\varphi_{\mathbf{z}}$ *the basis function associated with vertex* $\mathbf{z}$*, while*

$$\nu_T(\sigma_T, \mathbf{r}_{1,T}, f^E) = \Big(\sigma_T \mathbf{r}'_{1,T} G_T(f^E)\mathbf{r}_{1,T} + \frac{1}{\sigma_T}\mathbf{r}'_{2,T} G_T(f^E)\mathbf{r}_{2,T}\Big)^{1/2},$$

with G_T *the matrix in* (9)*.*

Proof By employing the Jacobian μ_h in (4), the definition (7) of the interpolant operator and the partition of unity property characterizing the set $\{\varphi_{\mathbf{z}}\}_{\mathbf{z}\in\mathcal{V}}$, we get

$$\begin{aligned}
\|f - I_h f^E\|_{L^1(\Gamma)} &= \int_\Gamma \big|f(\mathbf{x}) - I_h f^E(\mathbf{x})\big|\, d\Gamma \\
&= \int_{\Gamma_h} \big|f^E(\mathbf{x}) - I_h f^E(\mathbf{x})\big|\,\big|\mu_h(\mathbf{x})\big|\, d\Gamma_h \\
&= \int_{\Gamma_h} \Big|f^E(\mathbf{x}) - \sum_{\mathbf{z}\in\mathcal{V}} f^E_{\mathbf{z}}\varphi_{\mathbf{z}}(\mathbf{x})\Big|\,\big|\mu_h(\mathbf{x})\big|\, d\Gamma_h \\
&= \int_{\Gamma_h} \Big|\sum_{\mathbf{z}\in\mathcal{V}} \big(f^E(\mathbf{x}) - f^E_{\mathbf{z}}\big)\varphi_{\mathbf{z}}(\mathbf{x})\Big|\,\big|\mu_h(\mathbf{x})\big|\, d\Gamma_h \\
&\le \sum_{\mathbf{z}\in\mathcal{V}} \int_{\omega_{\mathbf{z}}} \big|f^E(\mathbf{x}) - f^E_{\mathbf{z}}\big|\,\big|\varphi_{\mathbf{z}}(\mathbf{x})\mu_h(\mathbf{x})\big|\, d\omega_{\mathbf{z}},
\end{aligned}$$

where the localization of the integral on Γ_h to $\omega_{\mathbf{z}}$ is due to the local support of $\varphi_{\mathbf{z}}$ coinciding with $\omega_{\mathbf{z}}$. Via Cauchy-Schwarz inequality and thanks to estimate (14), we derive

$$\begin{aligned}
&\|f - I_h f^E\|_{L^1(\Gamma)} \le \sum_{\mathbf{z}\in\mathcal{V}} \|f^E - f^E_{\mathbf{z}}\|_{L^2(\omega_{\mathbf{z}})}\|\varphi_{\mathbf{z}}\mu_h\|_{L^2(\omega_{\mathbf{z}})} \\
\le\ & C\sum_{\mathbf{z}\in\mathcal{V}} \|\varphi_{\mathbf{z}}\mu_h\|_{L^2(\omega_{\mathbf{z}})}\Big[\sum_{T\in\omega_{\mathbf{z}}} |T|\Big(\sigma_T \mathbf{r}'_{1,T} G_T(f^E)\mathbf{r}_{1,T} + \frac{1}{\sigma_T}\mathbf{r}'_{2,T} G_T(f^E)\mathbf{r}_{2,T}\Big)\Big]^{1/2}.
\end{aligned}$$

A reordering of the terms leads to the final result.

□

Remark 3.2 *The dependence of* ν_T *on* $\mathbf{r}_{2,T}$ *is implicit, due to the orthonormality of the singular vectors* $\mathbf{r}_{1,T}$ *and* $\mathbf{r}_{2,T}$*. Moreover, the constant involved in* (15) *is an actual number which does not imply any peculiar dependence, exactly as for the constant* C *in* (8)*.*

Remark 3.3 *The choice of the* $L^1(\Gamma)$*-norm to estimate the interpolation error is likely not the most standard one in the literature, where the* $L^2(\Gamma)$*- and the* $H^1(\Gamma)$*-norms are usually employed, both in an isotropic and in an anisotropic context (see, e.g., [8, 48, 1, 22, 28, 13, 17]). Nevertheless, as it is evident from the proof of estimate* (15)*, the* $L^1(\Gamma)$*-norm allows us to exploit the anisotropic Poincaré inequality in a straightforward way to bound the interpolation error.*

3.2 The geometric error

After deriving a theoretical tool to control the interpolation error in an anisotropic framework, we are now interested in controlling the error due to the fitting of the surface Γ via the polyhedral approximation Γ_h. Nevertheless, while estimate (15) is the result of a rigorous analysis, the estimate we propose for the geometric contribution is essentially heuristic. In more details, to quantify the mismatch between Γ and Γ_h, we resort to the signed distance function d whose zero level set coincides with Γ. In particular, the employment of the orthogonal projection $a(\cdot)$ in (1) to relate Γ and Γ_h via a bijection suggests us to identify the geometric error with the quantity $\|d - I_h d\|_{L^1(\Gamma)}$, after assuming sufficient regularity on function d. In some sense, we are supposing that the discrete surface Γ_h coincides with the zero level set of the function $I_h d$. In § 5.2.1, we provide a numerical justification to support this ansatz. Such an identification immediately leads us to provide an anisotropic estimate for the geometric error, simply by particularizing Proposition 2 to the distance function d.

Proposition 3 *Let $d : U_0 \to \mathbb{R}$ be the signed distance function associated with the implicit representation of the surface Γ and let us assume $d \in H^1(U_0)$. Then, there exists a constant C such that*

$$\|d - I_h d\|_{L^1(\Gamma)} \leq C \sum_{T \in \mathcal{T}_h} |T|^{1/2} \alpha_T \nu_T(\sigma_T, \mathbf{r}_{1,T}, d), \tag{16}$$

with α_T and $\nu_T(\sigma_T, \mathbf{r}_{1,T}, d)$ defined according to Proposition 2.

□

By comparing estimates (15) and (16), we remark that the distance function d does not require any extension via the projection operator $a(\cdot)$, since d is defined directly on the whole shell U_δ. Moreover, the regularity demanded on d is automatically guaranteed for smooth surfaces as the ones considered in § 5.2.

Other examples of geometric error control are available in the literature (see, e.g., [14, 12, 13, 25]). For instance, in [14] this control is a byproduct of the *a posteriori* residual-based error analysis developed for the problem of interest. In this case, an asymptotic analysis shows that the geometric error is a higher order term with respect to the discretization contribution.

Moving from Propositions 2 and 3, we define the *a priori* anisotropic error estimators

$$\eta_I = \sum_{T \in \mathcal{T}_h} \eta_{I,T} \quad \text{with} \quad \eta_{I,T} = |T|^{1/2} \alpha_T \nu_T(\sigma_T, \mathbf{r}_{1,T}, f^E)$$

and

$$\eta_G = \sum_{T \in \mathcal{T}_h} \eta_{G,T} \quad \text{with} \quad \eta_{G,T} = |T|^{1/2} \alpha_T \nu_T(\sigma_T, \mathbf{r}_{1,T}, d),$$

to control the interpolation and the geometric error, respectively. The two estimators share the same structure and both depend on the anisotropic geometric quantities. In § 5.2, we will numerically investigate the convergence rate of the two estimators η_I and η_G.

The next effort consists in conveniently combining the information associated with the function f and the surface Γ to drive the mesh adaptive procedure.

4 Merging the interpolation with the geometric error

The goal of this section is twofold. First, we propose a method suited to commute, separately, estimators η_I and η_G into an operative procedure to anisotropically adapt the mesh $\mathcal{T}_h$. Successively, we consider different techniques to merge the information provided by the two estimators. Actually, the global estimator $\eta_{IG} = \eta_I + \eta_G$ will be employed only to estimate the global error. To generate the adapted mesh, we will resort to a more intrinsic way via the concept of metric [27].

4.1 From the estimator to the metric

A metric associated with the surface $\Gamma \subset \mathbb{R}^3$ is a simmetric positive semi-definite tensor $\mathcal{M}_\Gamma : \Gamma \to \mathbb{R}^{3\times 3}$ identified, for each point $\mathbf{x} \in \Gamma$, by two strictly positive scalar functions $\rho_1 = \rho_1(\mathbf{x})$ and $\rho_2 = \rho_2(\mathbf{x})$ and by three vector functions $\mathbf{u}_1 = \mathbf{u}_1(\mathbf{x}), \mathbf{u}_2 = \mathbf{u}_2(\mathbf{x}), \mathbf{u}_3 = \mathbf{u}_3(\mathbf{x}) \in \mathbb{R}^3$ of unitary norm, such that $\mathbf{u}_i(\mathbf{x})\cdot\mathbf{u}_j(\mathbf{x}) = 0$ for any $\mathbf{x} \in \Gamma$ and for $i \neq j$, with $i, j = 1, 2, 3$. Thus, for each point $\mathbf{x} \in \Gamma$,

$$\begin{aligned}\mathcal{M}_\Gamma(\mathbf{x}) &= U(\mathbf{x})' R^{-2}(\mathbf{x}) U(\mathbf{x}) \\ &= \begin{bmatrix}\mathbf{u}_1(\mathbf{x}) & \mathbf{u}_2(\mathbf{x}) & \mathbf{u}_3(\mathbf{x})\end{bmatrix} \begin{bmatrix} 1/\rho_1^2(\mathbf{x}) & 0 & 0 \\ 0 & 1/\rho_2^2(\mathbf{x}) & 0 \\ 0 & 0 & 0 \end{bmatrix} \begin{bmatrix} \mathbf{u}_1'(\mathbf{x}) \\ \mathbf{u}_2'(\mathbf{x}) \\ \mathbf{u}_3'(\mathbf{x}) \end{bmatrix}.\end{aligned} \tag{17}$$

We remark that, since the diagonal matrix has rank at most equal to two, we can identify $\mathbf{u}_3$ with any vector function, for instance with the outward unit normal $\mathbf{n}$ to Γ at $\mathbf{x}$, coherently with the fact that the metric $\mathcal{M}_\Gamma(\mathbf{x})$ is defined on the plane tangent to Γ at $\mathbf{x}$.

Definition (17) may be particularized to a polyhedral surface $\Gamma_h \subset \mathbb{R}^3$, thus identifying the metric $\mathcal{M}_{\Gamma_h}$. In this context, it is rather standard to approximate $\mathcal{M}_{\Gamma_h}$ via a piecewise fuction, constant on each element T of Γ_h.

The actual goal now is, in some respect, the opposite one, i.e., the surface mesh Γ_h becomes the unknown. In particular, evaluating the estimators η_I, η_G on a background mesh, $\mathcal{T}_h^B$, we *predict* a metric $\mathcal{M}$, piecewise constant on $\mathcal{T}_h^B$, to generate a new adapted mesh, $\mathcal{T}_h^A$, which follows the directionalities of the function f and of the actual surface Γ with a desired accuracy. In more details, we define $\mathcal{M}$ such that $\mathcal{M}\big|_T = \mathcal{U}_T' \mathcal{R}_T^{-2} \mathcal{U}_T$ where, for any $T \in \mathcal{T}_h^B$, $\mathcal{U}_T = \begin{bmatrix}\mathbf{u}_{1,T}^* & \mathbf{u}_{2,T}^* & \mathbf{0}\end{bmatrix}' \in \mathbb{R}^{3\times 3}$ and $\mathcal{R}_T = \operatorname{diag}\big(\rho_{1,\mathrm{T}}^*, \rho_{2,\mathrm{T}}^*, 0\big) \in \mathbb{R}^{3\times 3}$. Then, starting from the predicted metric $\mathcal{M}$, we employ a metric-based adaptive procedure to build the mesh $\mathcal{T}_h^A$. Notice

that we have exploited the arbitrariness in the choice of $\mathbf{u}^*_{3,T}$, by identifying it with the vector identically equal to zero.

In the following, we detail the approach followed to derive the piecewise constant tensor $\mathcal{M}$, by extending the strategy proposed in [23] for the planar case to the context of a surface. In more details, we aim at minimizing the number of elements to be employed for guaranteeing a given solution accuracy by properly selecting the size, the shape and the orientation of each element. In addition, we demand that each element provides the same error by invoking a standard *equidistribution* criterion. To define $\mathcal{M}$, we refer to the generic anisotropic error estimator

$$\eta = \sum_{T \in \mathcal{T}_h} \eta_T \quad \text{with} \quad \eta_T = |T|^{3/2}\, \overline{\alpha}_T\, \overline{\nu}_T(\sigma_T, \mathbf{r}_{1,T}, g), \tag{18}$$

where

$$\overline{\nu}_T(\sigma_T, \mathbf{r}_{1,T}, g) = \left(\sigma_T \mathbf{r}'_{1,T} \overline{G}_T(g) \mathbf{r}_{1,T} + \frac{1}{\sigma_T} \mathbf{r}'_{2,T} \overline{G}_T(g) \mathbf{r}_{2,T}\right)^{1/2},$$

with g a generic $H^1(\Gamma)$-function, $\overline{\alpha}_T = \alpha_T/|T|^{1/2}$ and $\overline{G}_T = G_T/|T|$ the dimensionless counterpart of α_T and of the matrix G_T, respectively. In view of practical computations, estimator η will coincide with η_I ($g = f^E$) or η_G ($g = d$) or with a combination of them as detailed in the next section. Notice that, since both $\overline{\alpha}_T$ and $\overline{\Phi}_T$ are dimensionless, the information related to the area of T in (18) is essentially lumped in the factor $|T|^{3/2}$ (at least asymptotically).

Let `TOL` be the accuracy to be guaranteed via the generation of the adapted mesh $\mathcal{T}_h^A$. We demand that the local estimator η_T in (18) is such that

$$|T|^{3/2}\, \overline{\alpha}_T\, \overline{\nu}_T(\sigma_T, \mathbf{r}_{1,T}, g) = \frac{\texttt{TOL}}{\#\mathcal{T}_h^B}\,, \tag{19}$$

where $\#\mathcal{T}_h^B$ denotes the cardinality of the background grid. According to a predictive approach, we compute the quantities $\overline{\alpha}_T$, $|T| = |\widehat{T}| s_{1,T} s_{2,T}$, $\overline{G}_T(g)$ and $\#\mathcal{T}_h^B$ on the background grid, while σ_T and $\mathbf{r}_{1,T}$ become the actual unknowns. Thus, since on the right-hand side of (19) we have a constant value, the minimization of the number of mesh elements coincides with the maximization of the element area, i.e., with the minimization of the function $\overline{\nu}_T(\sigma_T, \mathbf{r}_{1,T}, g)$ with respect to σ_T and $\mathbf{r}_{1,T}$. As a consequence, for each element $T \in \mathcal{T}_h^B$, we solve the local constrained minimization problem:

$$\begin{cases} \text{find } \sigma_T^*, \mathbf{r}_{1,T}^* \text{ s.t. } \overline{\nu}_T(\sigma_T^*, \mathbf{r}_{1,T}^*, g) \text{ be minimized,} \\ \text{with } \sigma_T^* \geq 1 \text{ and } \mathbf{r}_{i,T}^* \cdot \mathbf{r}_{j,T}^* = \delta_{ij} \text{ for } i,j = 1,2. \end{cases} \tag{20}$$

The optimal value $\mathbf{r}_{2,T}^*$ for $\mathbf{r}_{2,T}$ is implicitly identified by the orthonormality relation between $\mathbf{r}_{1,T}$ and $\mathbf{r}_{2,T}$. The minimization problem (20) can be explicitly

solved with straightforward computations, without demanding an extra computational burden. Indeed, following [38], we obtain

$$\mathbf{r}^*_{1,T} = \mathbf{w}_{2,T}, \quad \mathbf{r}^*_{2,T} = \mathbf{w}_{1,T}, \quad \sigma^*_T = \frac{(\mu_{1,T})^{1/2}}{(\mu_{2,T})^{1/2}}, \tag{21}$$

where $\big(\mu_{i,T}, \mathbf{w}_{i,T}\big)$, with $i = 1, 2$, are the eigenvalue-eigenvector pairs of the matrix $\overline{G}_T(g)$, with $\mu_{1,T} \geq \mu_{2,T}$. This provides the optimal value $2^{1/2}\left(\mu_{1,T}\mu_{2,T}\right)^{1/4}$ for $\overline{\nu}(\sigma^*_T, \mathbf{r}^*_{1,T}, g)$ which does not depend anymore on the aspect ratio. The equidistribution constraint in (19) leads us to find separately the two optimal anisotropic lengths $s^*_{1,T}$ and $s^*_{2,T}$ whose ratio coincides with σ^*_T in (21). In more details, solving the equations

$$|\widehat{T}|^{3/2}\left(s^*_{1,T}\, s^*_{2,T}\right)^{3/2}\overline{\alpha}_T\, 2^{1/2}\left(\mu_{1,T}\,\mu_{2,T}\right)^{1/4} = \frac{\texttt{TOL}}{\#\mathcal{T}^B_h}\,, \qquad \frac{s^*_{1,T}}{s^*_{2,T}} = \frac{\mu^{1/2}_{1,T}}{\mu^{1/2}_{2,T}}\,,$$

we get

$$s^*_{1,T} = \left(\frac{1}{2^{1/2}}\left(\frac{\mu_{1,T}}{\mu^2_{2,T}}\right)^{1/2}\frac{\texttt{TOL}}{\#\mathcal{T}^B_h\,\overline{\alpha}_T\,|\widehat{T}|^{3/2}}\right)^{1/3}, \tag{22}$$

$$s^*_{2,T} = \left(\frac{1}{2^{1/2}}\left(\frac{\mu_{2,T}}{\mu^2_{1,T}}\right)^{1/2}\frac{\texttt{TOL}}{\#\mathcal{T}^B_h\,\overline{\alpha}_T\,|\widehat{T}|^{3/2}}\right)^{1/3}. \tag{23}$$

Thus, the optimal metric $\mathcal{M}$ turns out to be defined via the elemental matrices $\mathcal{M}\big|_T = \mathcal{U}'_T\mathcal{R}_T^{-2}\mathcal{U}_T$, with

$$\mathcal{U}_T = \big[\mathbf{u}^*_{1,T}\ \ \mathbf{u}^*_{2,T}\ \ \mathbf{0}\big]', \quad \mathcal{R}_T = \mathrm{diag}\big(\rho^*_{1,\mathrm{T}}, \rho^*_{2,\mathrm{T}}, 0\big), \tag{24}$$

where $\mathbf{u}^*_{i,T} = \mathbf{r}^*_{i,T}$, $\rho^*_{i,T} = s^*_{i,T}$, for $i = 1, 2$, according to definition (21) and (22)-(23), respectively. Finally, the metric $\mathcal{M}$ is employed to generate the new adapted mesh $\mathcal{T}^A_h$ via the procedure detailed in § 5.1.

Remark 4.1 *As an alternative to the minimization of the number of mesh elements for a fixed solution accuracy, we might fix the cardinality of the mesh while maximizing the accuracy of the approximation. Similar computations lead to identify the optimal metric $\mathcal{M}$ also in this case. Essentially, the tolerance* TOL *involved in the computation of the optimal values $\mathbf{u}^*_{i,T}$, $\rho^*_{i,T}$ has to be modified.*

4.2 Combination of metrics

Before detailing the adaptation procedure, we consider the issue of dealing, a priori, with two different metrics $\mathcal{M}_I$ and $\mathcal{M}_G$ associated with estimator η_I and η_G, respectively. Both these metrics are computed starting from the same background grid $\mathcal{T}^B_h$, i.e., for each element $T \in \mathcal{T}^B_h$, we have two predictions for the optimal size, shape and orientation provided by the matrices $\mathcal{U}^I_T = \big[\mathbf{u}^{I,*}_{1,T}\ \ \mathbf{u}^{I,*}_{2,T}\ \ \mathbf{0}\big]'$,

$\mathcal{R}_T^I = \mathrm{diag}\big(\rho_{1,\mathrm{T}}^{\mathrm{I},*}, \rho_{2,\mathrm{T}}^{\mathrm{I},*}, 0\big)$ and $\mathcal{U}_T^G = \big[\mathbf{u}_{1,T}^{G,*}\ \ \mathbf{u}_{2,T}^{G,*}\ \ \mathbf{0}\big]'$, $\mathcal{R}_T^G = \mathrm{diag}\big(\rho_{1,\mathrm{T}}^{\mathrm{G},*}, \rho_{2,\mathrm{T}}^{\mathrm{G},*}, 0\big)$ yielded by the minimization problem (20) for $g = f^E$ and $g = d$, respectively when combined with the equidistribution of the error.
The role played by $\mathcal{M}_I$ and $\mathcal{M}_G$ is completely different: $\mathcal{M}_I$ is instrumental to control the error related to the function f, while $\mathcal{M}_G$ is meant to limit the error due to the approximation of Γ via Γ_h. Ideally, we aim at controlling both these error sources. The idea is to combine metrics $\mathcal{M}_I$ and $\mathcal{M}_G$ to get both benefits. For this purpose, we investigate three different techniques, according to which the metric $\mathcal{M}_{IG}$ driving the adaptive procedure coincides with:

a) the *metric intersection* $\mathcal{M}_{IG}^{\cap} \equiv \mathcal{M}_I \cap \mathcal{M}_G$, based on the simultaneous reduction of the metrics $\mathcal{M}_I$ and $\mathcal{M}_G$ (we refer to Chapt. 10 in [27] for the technical details). This approach represents the most straightforward way to merge the discretization with the geometric error control even though, in some circumstances, the results tend to be overly conservative since the intersection of two anisotropic metrics does not necessarily yield an anisotropic metric $\mathcal{M}_{IG}^{\cap}$ (see Figure 3 for an example);

b) the *maximum metric* $\mathcal{M}_{IG}^{\max}$, such that $\mathcal{M}_{IG}^{\max}\big|_T$ is the metric associated with the maximum local estimator between $\eta_{I,T}$ and $\eta_{G,T}$, for any $T \in \mathcal{T}_h^B$;

c) a *convex combination* of the two metrics $\mathcal{M}_I$ and $\mathcal{M}_G$. In particular, we start from the convex combination $\gamma\eta_{I,T} + (1-\gamma)\eta_{G,T}$ of the local estimators with $\gamma \in [0,1]$. Then, following Proposition 5.4 in [37], we advantageously exploit the common structure shared by $\eta_{I,T}$ and $\eta_{G,T}$ to combine them into the single estimator

$$\eta_{IG,T}^{\gamma} = |T|^{3/2}\,\overline{\alpha}_T\,\overline{\nu}_T^{\gamma}(\sigma_T, \mathbf{r}_{1,T}, f^E, d), \tag{25}$$

where

$$\overline{\nu}_T^{\gamma}(\sigma_T, \mathbf{r}_{1,T}, f^E, d) = \Big(\sigma_T \mathbf{r}_{1,T}' \overline{G}_T^{\gamma}(f^E, d)\mathbf{r}_{1,T} + \frac{1}{\sigma_T}\mathbf{r}_{2,T}' \overline{G}_T^{\gamma}(f^E, d)\mathbf{r}_{2,T}\Big)^{1/2}$$

with $\overline{G}_T^{\gamma}(f^E, d) = \gamma^2\,\overline{G}_T(f^E) + (1-\gamma)^2\,\overline{G}_T(d)$. At this point, by mimicking the procedure employed to convert estimator (18) into the optimal metric identified by (24), we get the metric $\mathcal{M}_{IG}^{\gamma}$, automatically blending the interpolation with the geometric information.

We remark that approach c) allows us to skip the computation of the two distinct optimal metrics $\mathcal{M}_I$ and $\mathcal{M}_G$. A single optimal metric is derived after defining the new error estimator $\eta_{IG}^{\gamma} = \sum_{T \in \mathcal{T}_h^B} \eta_{IG,T}^{\gamma}$ with $\eta_{IG,T}^{\gamma}$ as in (25).

Independently of the approach followed to get metric $\mathcal{M}_{IG}$, we eventually deal with an elemental predicted metric $\mathcal{M}_{IG}\big|_T$, for each element of the background grid $\mathcal{T}_h^B$. This elementwise anisotropic information will drive the adaptive procedure.

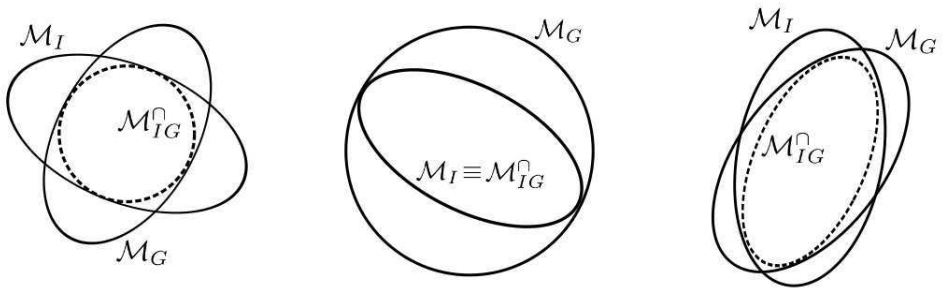

Figure 3: Examples of mesh intersection $\mathcal{M}_I \cap \mathcal{M}_G$.

In § 5.2 we numerically investigate the different approaches a)-c) by comparing the corresponding performances.

5 Numerical assessment

This section illustrates the algorithmic and computational kernel of the paper. After setting the adaptive procedure to commute $\mathcal{M}_{IG}$ into practical operations yielding the adapted mesh $\mathcal{T}_h^A$, we consider two test cases to investigate the robusteness of the proposed adaptive tool.

5.1 The adaptive procedure

To generate the mesh $\mathcal{T}_h^A$, we adopt a metric-based adaptive procedure, a standard approach in an anisotropic framework (see, e.g., [25, 23, 10, 43, 4]), since, as detailed in the previous section, a metric exactly collects all the information needed to uniquely identify size, shape and orientation of a generic triangle T. The optimal goal is to obtain a mesh $\mathcal{T}_h^A$ such that each element $T \in \mathcal{T}_h^A$ coincides with a unitary equilateral triangle with respect to the metric $\mathcal{M}_{IG}$, i.e, $\|e\|_{\mathcal{M}_{IG}} = 1$, for any $e \in T$ and for any $T \in \mathcal{T}_h^A$, with $\|e\|_{\mathcal{M}_{IG}} = \sqrt{e' \mathcal{M}_{IG}\, e}$. Clearly, this target is not exactly reachable in a general case. We devise an optimization procedure to minimize the distance of the adapted grid to the optimal one, in a sense that is described in the following.

We resort to the following multi-choice criterion: for any edge e of the skeleton $\mathcal{E}_B$ of the background grid $\mathcal{T}_h^B$,

i) if $\|e\|_{\mathcal{M}_{IG}} \simeq 1$, the edge e already has the optimal length with respect to the predicted metric and can be directly identified with an edge of the adapted mesh $\mathcal{T}_h^A$;

ii) if $\|e\|_{\mathcal{M}_{IG}} \gg 1$, the edge e is too long according to the predicted metric;

iii) if $\|e\|_{\mathcal{M}_{IG}} \ll 1$, the edge e is too short according to the predicted metric.

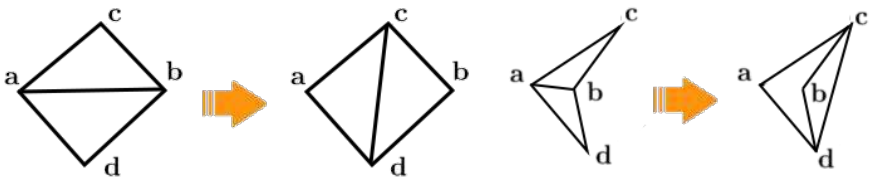

Figure 4: Swapping of the edge ab (left); instance of unswappable edge ab (right).

In both the cases ii) and iii), the edge e cannot be assumed as definitive but it has to be properly modified before being included in $\mathcal{T}_h^A$. For this purpose, we employ an iterative procedure based on local operations. The meshes playing the role of background and adapted grid clearly update during the iterative process.

To compute the length $\|e\|_{\mathcal{M}_{IG}}$ starting from the elemental metrics $\mathcal{M}_{IG}\big|_T$, we first assign a metric $\mathcal{M}_{IG}^{\mathbf{z}}$ to each node $\mathbf{z}$ of the current mesh, by computing the mean of the metrics associated with the triangles of the patch $\omega_{\mathbf{z}}$. Then, let $\mathbf{a}$ and $\mathbf{b}$ be the endpoints of the edge e and let $\mathcal{M}_{IG}^{\mathbf{a}}$ and $\mathcal{M}_{IG}^{\mathbf{b}}$ be the corresponding metrics. We compute

$$\|e\|_{\mathcal{M}_{IG}} = \max\left(\|e\|_{\mathcal{M}_{IG}^{\mathbf{a}}}, \|e\|_{\mathcal{M}_{IG}^{\mathbf{b}}}\right),$$

where $\|e\|_{\mathcal{M}_{IG}^{\mathbf{z}}} = \sqrt{e' \mathcal{M}_{IG}^{\mathbf{z}} e}$ for $\mathbf{z} = \mathbf{a}, \mathbf{b}$.

The section is organized as follows. Section 5.1.1 itemizes the local operations used to ensure criterion i) for each edge of the final adapted mesh, while in § 5.1.2 we fix a precise sequence of local operations to set the adaptive procedure. This represents a first attempt to combine the anisotropic error analysis based on the theory in [22, 23] with an adaptive procedure exploiting local operations. Moreover, we remark that, since we have a unique metric merging the information related to function f and to the surface fitting, we are relieved from distinguishing in the adaptive algorithm two distinct phases to control the different errors.

5.1.1 Local operations

We use four different operations.

A. Edge swapping Edge swapping turns out to be among the most efficient and effective local operations to anisotropically modify a generic triangular mesh [24, 5]. Edge swapping works on pairs of adjacent triangles sharing a common edge, e.g., triangles $\Delta_{\mathbf{abc}}$, $\Delta_{\mathbf{bad}}$ in Figure 4, left which share the edge $\mathbf{ab}$. The effect of such an operation is to replace these two triangles with the new ones $\Delta_{\mathbf{acd}}$ and $\Delta_{\mathbf{cdb}}$, simply by considering the edge $\mathbf{cd}$ instead of the original one $\mathbf{ab}$. In the 2D planar case this ensures that the area portion occupied by the original elements is preserved after the swapping.

It is not always possible to apply an edge swapping even in a planar framework. With reference to Figure 4, we can swap the edge $\mathbf{ab}$ if the following conditions are verified:

R1) the edge $\mathbf{cd}$ does exist in the mesh (the meaning of this condition is clarified in the next section);

R2) there does not exist an obtuse angle adjacent to the edge $\mathbf{ab}$. Figure 4, right furnishes an example of unswappable edge. The new edge $\mathbf{cd}$ leads to occupy a portion of the domain area before not included in $\Delta_{\mathbf{abc}} \cup \Delta_{\mathbf{bad}}$. Moreover, the conformity of the mesh is compromised.

The edge swapping becomes a more complex operation when dealing with a triangular surface mesh, due to the intrinsic curvature of the surface. This is particularly troublesome where the mesh exhibits ridges. As exemplified in Figure 5, left an edge swapping may lead to an incorrect approximation of the surface, by violating the corresponding curvature. To overcome this issue, an additional condition is checked besides the two previous ones:

R3) the angle θ between the normals to the faces $\Delta_{\mathbf{abc}}$ and $\Delta_{\mathbf{bad}}$ is smaller than a minimum threshold θ_{min} (in the numerical validation below, we set $\theta_{min} = 15°$).

After stating the geometric and topological consistency of the edge swapping operation, we fix the following criterion in view of the mesh adaptation: we swap the edge $\mathbf{ab}$ if

$$\Big|\, ||\mathbf{cd}||_{\mathcal{M}_{IG}} - 1 \Big| < \Big|\, ||\mathbf{ab}||_{\mathcal{M}_{IG}} - 1 \Big|, \tag{26}$$

i.e., if the length predicted by the metric $\mathcal{M}_{IG}$ for the edge $\mathbf{cd}$ is closer to one compared with the length of $\mathbf{ab}$.

Due to the important role played by the edge swapping in view of an anisotropic mesh adaptation, we have settled a new edge swapping routine starting from the well-known Lawson flip algorithm for the construction of a two-dimensional planar

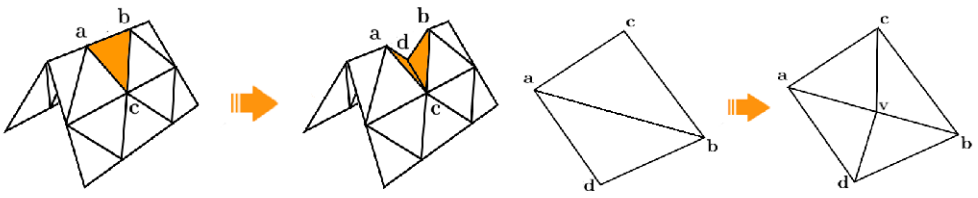

Figure 5: Example of a not allowed edge swapping, yielding a distorted approximation of the original ridge (left); splitting of the edge $\mathbf{ab}$ (right).

Delaunay triangulation [36]. In particular, we modify the original algorithm to deal with surface meshes and to include the metric-based check (26).

To start the edge swapping algorithm we need two stacks, S and S_1. At the beginning, the stack S contains all the edges to be checked, while S_1 is an empty stack which gradually collects the currently non swappable edges. The algorithm may be applied globally, i.e., to all the edges of the current grid, or just locally, namely to a subset of elements. For the sake of simplicity, we refer to the configuration in Figure 4, left by assuming that, at the beginning, S cointains only the edge $\mathbf{ab}$.

Thus, the variant we proposed for the Lawson flip algorithm reads as:

Edge swapping algorithm

`EdgeSwap`(S, S_1)

```
 1: while (S is non-empty) do
 2:   count = 0;
 3:   while (S is non-empty) do
 4:     pop ab from S;
 5:     if (cd does meet conditions R1) and (26)) then
 6:       if (ab does meet conditions R2) and R3)) then
 7:         flip ab into cd;
 8:         for (xy ∈ {ac, cb, bd, da}) do
 9:           push xy into S;
10:         end for
11:         count = count + 1;
12:       else
13:         push ab into S1;
14:       end if
15:     end if
16:   end while
17:   if (S1 is non-empty and count > 0) then
18:     swap S and S1;
19:   end if
20: end while
```

Essentially, we may distinguish an inner (lines 3-16) and and external (lines 17-19) loop. In the inner loop, as it is standard according to the Lawson procedure, the check for the swapping propagates from the edges contained from the beginning in S and which are recognized as swappable to the corresponding neighbouring edges. The three topological criteria R1)-R3) and the metric check (26) have to be satisfied to consider an edge as swappable. In particular, if the edge $\mathbf{ab}$ does not meet criteria R2) and R3) even though the edge $\mathbf{cd}$ satisfies conditions R1) and (26), the edge $\mathbf{ab}$ is automatically moved to stack S_1. The `EdgeSwap` algorithm is such that, once an edge has been swapped, it will never be re-generated. Nevertheless, before closing the procedure, the external loop performs an additional

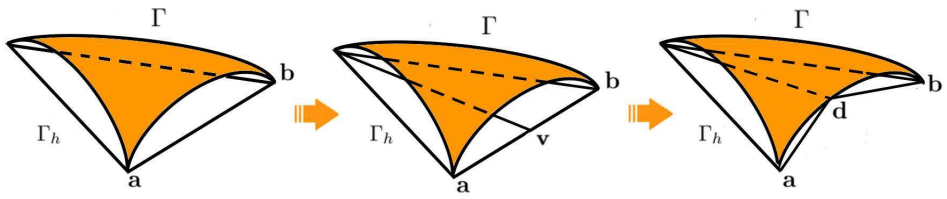

Figure 6: Splitting of the edge $\mathbf{ab}$ via the addition of the point $\mathbf{v}$ and projection of $\mathbf{v}$ on the surface Γ via point $\mathbf{d}$.

check on the edges previously discarded since identifying a non valid topological configuration even though leading to an improvement in terms of metric.

Numerical experiments show that algorithm `EdgeSwap` is very efficient. As detailed in the next section, we employ this algorithm in a combined way, i.e., each time we locally modify the mesh, we push the edges involved by this operation into the stack S and we employ function `EdgeSwap`. Successively, the edge swapping is applied to the whole mesh to make the $\mathcal{M}_{IG}$-lenght of each edge as close as possible to the unitary value.

B. Edge splitting This operation plays an important role in view of a local refinement of the mesh. The idea is to increase the mesh resolution where the solution exhibits strong variations, by locally reducing the size of the mesh and by stretching the elements according to the directional features of the solution.
First, we identify the edges to be split, i.e., the edges whose length predicted via the metric $\mathcal{M}_{IG}$ is greater than one. Then, we halve each of these edges by inserting a new vertex at the corresponding midpoint. With reference to Figure 5, right, if the edge $\mathbf{ab}$ is classified as a too long edge, we replace the two faces $\Delta_{\mathbf{abc}}$ and $\Delta_{\mathbf{bad}}$ with the four faces $\Delta_{\mathbf{avc}}$, $\Delta_{\mathbf{vcb}}$, $\Delta_{\mathbf{vbd}}$, $\Delta_{\mathbf{vda}}$ by adding the new vertex $\mathbf{v}$ at the midpoint of $\mathbf{ab}$.
An extra care has to be taken since we are dealing with a polyhedral surface. As depicted in Figure 6, center the addition of the new vertex $\mathbf{v}$ does not necessarily lead to an improvement in fitting Γ via the discrete surface Γ_h. As a consequence, after the addition of the new vertex, we project $\mathbf{v}$ on the surface Γ by resorting to the algorithm proposed in [32]. This simple device necessarily yields an effective improvement in the approximation of Γ as shown in Figure 6, right.

C. Edge collapsing Mesh coarsening pursues the opposite goal with respect to mesh refinement, namely the mesh elements are properly enlarged where the solution exhibits a smooth behaviour. The most significative operation in view of a mesh coarsening is the edge collapsing which represents, in some sense, the inverse operation to the edge splitting. In more details, to perform the edge collapsing, we resort to an edge contraction technique ([34, 35, 44]), after identifying a too short

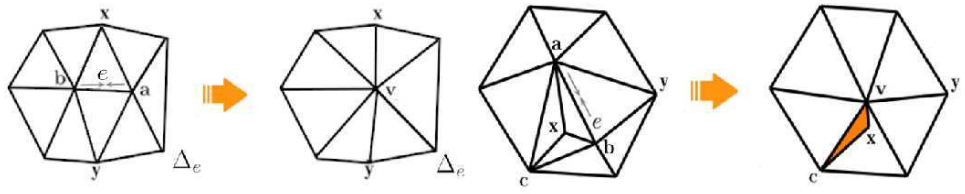

Figure 7: Contraction of the edge e into the vertex $\mathbf{v}$ (left); example of invalid topological configuration yielded by the contraction of the edge e (right).

edge, namely an edge e with $\|e\|_{\mathcal{M}_{IG}} \ll 1$. With reference to Figure 7, left we contract the edge e by progressively moving vertex $\mathbf{a}$ towards vertex $\mathbf{b}$ until they both coincide with vertex $\mathbf{v}$. The faces $\Delta_{\mathbf{bax}}$ and $\Delta_{\mathbf{bay}}$ are removed by the contraction, thus reducing the cardinality of the patch Δ_e while preserving the covered area and the conformity of the mesh.

Different choices are possibile to fix the position of the vertex $\mathbf{v}$. We usually select the midpoint of the edge to be contracted unless this choice does lead to invalid topological configurations, e.g., to inverted triangles characterized by a negative area. Figure 7, right exemplifies such a possibility. Following [18], to overcome this issue we make an additional check on the vertices connected to the endpoints of the edge e, i.e., on the sets of vertices connected to $\mathbf{a}$ and $\mathbf{b}$, respectively. In particular, if the intersection between these two sets includes any point different from the vertices of the faces $\Delta_{\mathbf{bax}}$ and $\Delta_{\mathbf{bay}}$, the contraction of the edge $\mathbf{ab}$ into the vertex $\mathbf{v}$ leads to an inverted triangle. In the specific case of Figure 7, right, the presence of the point $\mathbf{c}$ justifies the failure of the contraction algorithm.

Of course, other techniques may be exploited to avoid these incorrect configurations as well as to select the vertex $\mathbf{v}$ (see, e.g., [26, 15, 11]). Exactly as for the edge splitting, after any edge contraction we have to project the new position of the vertex $\mathbf{v}$ on the surface Γ to actually guarantee the fitting of the surface at hand.

D. Node smoothing Node smoothing is a standard method to improve the quality of a mesh. In contrast to the previous ones, this operation simply moves the nodes of the mesh in new positions without modifying the mesh topology. We may provide a physical interpretation of this operation, by identifying the patch $\Delta_{\mathbf{v}}$ of elements associated with the vertex $\mathbf{v}$ with a system of springs (see Figure 8, left). In particular, the smoothing procedure aims at locating the vertex $\mathbf{v}$ in the position that minimizes the elastic energy of the whole system. In an isotropic context, the smoothing moves $\mathbf{v}$ to the barycenter of $\Delta_{\mathbf{v}}$. On the contrary, when dealing with an anisotropic mesh adaptation, we have to properly include the effect of the metric, for instance by varying the stiffness coefficient of the different springs.

Exactly as for the edge collapsing, the new position for the point $\mathbf{v}$ may lead to invalid configurations as dipicted in Figure 8, right where inverted elements

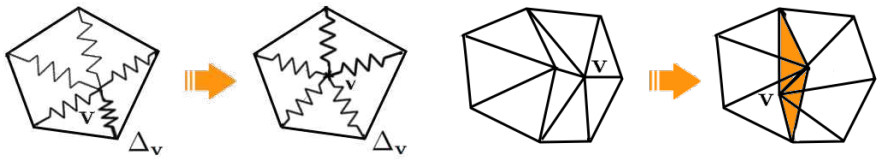

Figure 8: Node smoothing: example of valid (left) and of not valid (right) configuration.

are generated by the smoothing of $\mathbf{v}$. As a consequence, a careful check on the predicted new configuration is performed before applying any smoothing.

5.1.2 The adaptation sequence

The iterative procedure that leads to the generation of the optimal mesh with $||e||_{\mathcal{M}_{IG}} \approx 1$, might be strongly affected by the selected sequence of local operations to be applied to the initial mesh.

We resort to the following strategy. Essentially, the edge splitting and the edge collapsing operations, in combination with a local edge swapping and followed by a global edge swapping, are iteratively repeated together with a cycle of runs of node smoothing.
The iterative procedure is controlled by three different checks, involving the tolerance `TOL` assigned by the user on the approximation accuracy, a maximum allowed number `maxIter` of adaptive iterations, and a check on the cardinality of the mesh. In practice, these controls are carried out by introducing three flag variables, i.e.,

FL1) `errCheck` : if the global error evaluated on the new adapted mesh via the quantity $\eta_{IG} = \eta_I + \eta_G$ is greater than `TOL`, `errCheck` is set `true`, otherwise it is `false`;

FL2) `iterCheck` : the value of this flag is `true` until the number of iterations is lower than `maxIter`;

FL3) `meshCheck` : we compute the value

$$\#\mathcal{T}_{\text{diff}} = \frac{|\#\mathcal{T}_{\text{old}} - \#\mathcal{T}_{\text{new}}|}{\#\mathcal{T}_{\text{old}}},$$

where $\#\mathcal{T}_{\text{old}}$ and $\#\mathcal{T}_{\text{new}}$ denotes the cardinality of the mesh before and after the adaptation, respectively. Then, if $\#\mathcal{T}_{\text{diff}} > 0.05$, `meshCheck` is set `true`, otherwise it is `false`.

The check based on the last flag is essentially meant to stop the adaptive procedure when the number of elements involved by the local operations becomes too small (less than 5% of the cardinality of the current mesh) to significantly improve the

quality of the approximate solution $f_h = I_h f^E$ as well as of the surface fitting provided by $I_h d$.

Thus, the whole adaptive algorithm reads as follows:

Mesh adaptation algorithm

`MeshAdaptation(TOL, maxIter)`

1: `set errCheck=`**`true`**`, iterCheck=`**`true`**`, meshCheck=`**`true`**;
2: `count=1`;
3: **while** (`errCheck && iterCheck && meshCheck`) **do**
4: `compute the metric` $\mathcal{M}_{IG}$ `associated with tolerance TOL`;
5: `split the edges s.t.` $||e||_{\mathcal{M}_{IG}} > 1.5$; `local edge swapping`;
6: `global edge swapping`;
7: `collapse the edges s.t.` $||e||_{\mathcal{M}_{IG}} < 0.5$; `local edge swapping`;
8: `global edge swapping`;
9: **for** $k \in \{1, ..., 5\}$ **do**
10: `smooth all the vertices; local edge swapping`;
11: `global edge swapping`;
12: **end for**
13: `count=count+1`;
14: `update errCheck, iterCheck, meshCheck`;
15: **end while**

The adaptive procedure stops when one of the three flags FL1)-FL3) assumes the value `false`. We highlight the intensive employment of the function `EdgeSwap`, both at a local (lines 5, 7, 10) and at a global (lines 6, 8, 11) level, in accordance with the aim of generating an anisotropic mesh. Finally, the number of node smoothing iterations is heuristically set via a simple trial-and-error procedure.

The meaning of request R1) should be clear in the light of the whole adaptive procedure. Since the swapping quickly propagates to the edges of the mesh, an edge marked as swappable might be previously involved by other operations before swappig actually takes place.

5.2 Test cases

In this section we investigate the robustness of the error analysis as well as of the adaptive procedure set in the previous sections on both an open and a closed surface. Starting from the same initial grid, we compare the adapted meshes generated via four different choices of the metric, namely, the three metrics $\mathcal{M}_{IG}^{\cap}$, $\mathcal{M}_{IG}^{\max}$, $\mathcal{M}_{IG}^{\gamma}$ defined in § 4.2 together with the metric $\mathcal{M}_I$ taking into account the interpolation error only. A more quantitative investigation of the anisotropic analysis is also provided.

5.2.1 Test case 1: an open surface

We consider the sinusoidal surface Γ_1 defined by the signed distance function $d_1 : [0,1] \times [0,1] \times [-0.2, 0.2] \to \mathbb{R}$ such that

$$d_1(\mathbf{x}) = d_1(x_1, x_2, x_3) = 0.2 \cos(\pi x_1) \cos(\pi x_2) - x_3,$$

and the function $f_1 : \Gamma_1 \to \mathbb{R}$ with

$$f_1(\mathbf{x}) = f_1(x_1, x_2, x_3) = 4x_2(1 - x_1)(1 - x_2)(1 - e^{-1000x_1}).$$

Figure 9 depicts the colorplot of function f_1 on Γ_1. The solution exhibits a boundary layer along the edge $\{(0, x_2),\ 0 \leq x_2 \leq 1\}$, where it reaches its maximum value (see the highlighted area in the figure).

We run the adaptive procedure by making different choices for the metric $\mathcal{M}_{IG}$. In particular, in algorithm `MeshAdaptation`, we set `TOL` = 6.e-05, `maxIter`= 10 while we choose the value $2/3$ for the parameter γ combining the interpolation and the geometric metrics.

Comparison among metrics Figure 10 compares a detail of the adapted grids associated with the metric $\mathcal{M}_{IG}^{\cap}$, $\mathcal{M}_{IG}^{\max}$, $\mathcal{M}_{IG}^{\gamma}$ and $\mathcal{M}_I$, respectively which are constitued by a similar number (about 8700) of elements. In particular, we focus on the boundary layer, i.e., on a critical region to be described. The layer is correctly detected by all the metrics and the elements are properly stretched. Nevertheless, the anisotropic features of the mesh are significantly less evident when the metric intersection drives the adaptive procedure (compare, e.g., Figure 10 (a) with Figure 10 (b)). This is confirmed by the maximum value $\sigma_{\max} = \max_{T \in \mathcal{T}_h^A} \sigma_T$ of

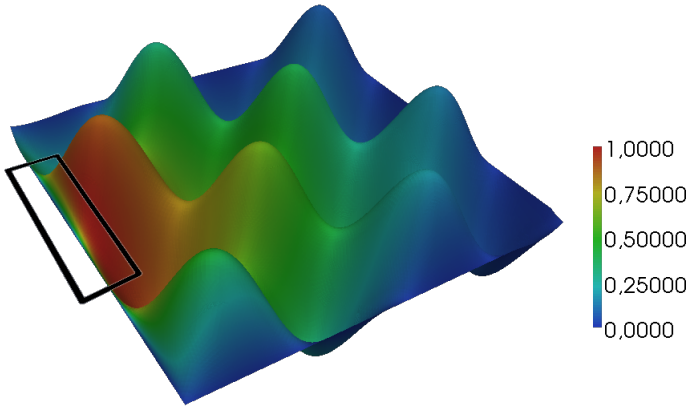

Figure 9: Test case 1: function f_1 on the surface Γ_1 (highlighted the boundary layer).

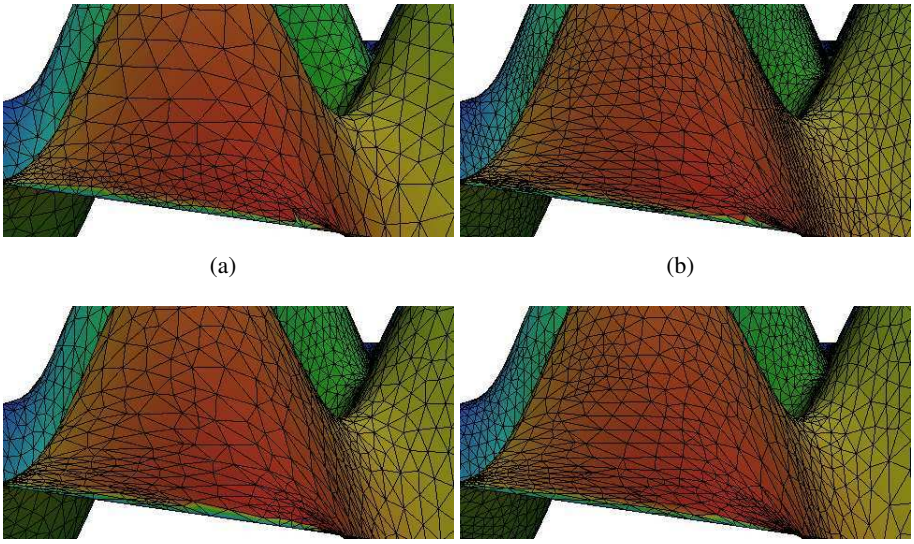

Figure 10: Test case 1: detail in correspondence with the boundary layer of the adapted mesh $\mathcal{T}_h^A$ generated via the metric (a) $\mathcal{M}_{IG}^{\cap}$, (b) $\mathcal{M}_{IG}^{\max}$, (c) $\mathcal{M}_{IG}^{\gamma}$ and (d) $\mathcal{M}_I$.

the corresponding aspect ratios, which is collected in the second column of Table 1. Notice that also the mesh in Figure 10 (d) obtained by exploiting the information associated only with the interpolation error exhibits elements correctly stretched, with a maximum aspect ratio comparable with the one associated with $\mathcal{M}_{IG}^{\max}$.
The benifits led by the inclusion of the geometric information in the adaptive procedure become evident if we drastically diminish the number of the elements in the adapted mesh (i.e., if we increase the value of `TOL`). As Figure 11 (d) shows, the quality of the approximation provided by $\mathcal{M}_I$ may become very poor in such a case. The four adapted meshes are generated after fixing a tolerance `TOL` = 8e-04 and are characterized by a number of elements about equal to 2600. Metric $\mathcal{M}_I$ is not able to correctly describe surface Γ_1 with an evident loss of accuracy, for instance, in detecting the peak of Γ_1 located at the corner $(1, 1)$. On the contrary, despite the limited number of elements, the geometric information integrated in the metrics $\mathcal{M}_{IG}^{\cap}$, $\mathcal{M}_{IG}^{\max}$, $\mathcal{M}_{IG}^{\gamma}$ are enough to meet the main geometric characteristics of the exact surface. The best approximation in terms of geometry fitting turns out to be the one associated with $\mathcal{M}_{IG}^{\max}$, as confirmed by the values in the third column of Table 1, where the quantity $d_{\max} = \max_{K \in \mathcal{T}_h^A} \|p_K - b_K\|_2$, measuring the mismatch between Γ_1 and $\mathcal{T}_h^A$ is gathered for the four meshes in Figure 11, with b_K the barycenter of the triangle K and p_K the corresponding projection on the surface Γ_1, $\|\cdot\|_2$ denoting the standard Euclidean norm. As expected the largest value of $d_{\max}$ is associated with the mesh predicted via $\mathcal{M}_I$.

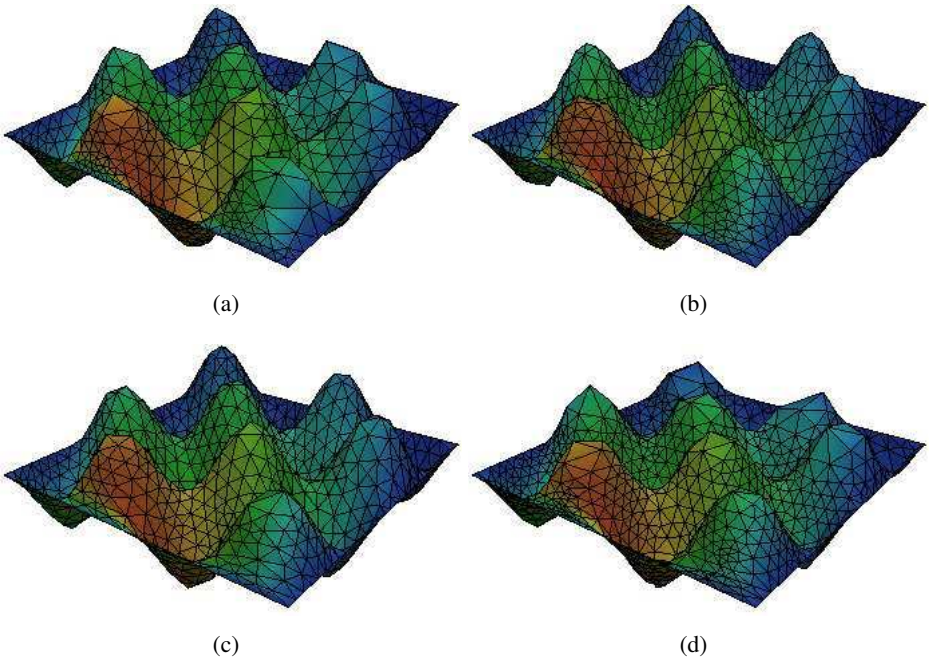

(a) (b) (c) (d)

Figure 11: Test case 1: adapted mesh $\mathcal{T}_h^A$ generated via the metric (a) $\mathcal{M}_{IG}^{\cap}$, (b) $\mathcal{M}_{IG}^{\max}$, (c) $\mathcal{M}_{IG}^{\gamma}$ and (d) $\mathcal{M}_I$.

Anisotropy versus isotropy We check the computational advantages led by an anisotropic mesh adaptation with respect to an isotropic procedure. This represents a statement well-established in the literature (see, e.g., [6, 7, 37, 42, 47]). To make this analysis quantitative, we introduce the following definitions

$$e_{\text{tot}} = \|f - I_h f^E\|_{L^1(\Gamma)}, \quad e_{\text{mean}} = \frac{e_{\text{tot}}}{|\mathcal{T}_h^A|}, \quad e_{\max} = \max_{T \in \mathcal{T}_h^A} ||f - I_h f^E||^*_{L^1(T)}. \tag{27}$$

In particular, to compute e_{tot}, we employ the equality

$$\|f - I_h f^E\|_{L^1(\Gamma)} = \int_{\Gamma_h} \left| f^E(\mathbf{x}) - I_h f^E(\mathbf{x}) \right| \left| \mu_h(\mathbf{x}) \right| d\Gamma_h \tag{28}$$

stated in the proof of Proposition 2, whereas

$$||f - I_h f^E||^*_{L^1(T)} = \int_T \left| f^E(\mathbf{x}) - I_h f^E(\mathbf{x}) \right| \left| \mu_h(\mathbf{x}) \right| dT$$

deriving by a localization of (28) to the mesh face T. First, we verify that anisotropy provides an improvement in terms of accuracy when we fix the cardinality of the adapted mesh. Table 2 exemplifies such a trend. We have excluded from this comparison the adaptive procedure based on the intersection of metrics due to the poor performances of this approach in terms of anisotropy. While a not so striking difference on the maximum error is obtained, we appreciate a reduction of at least one third or more on the total error as well as a gain of one order on the mean error.

metric	$\sigma_{\max}$	$d_{\max}$
$\mathcal{M}_{IG}^{\cap}$	4.93	7.923e-03
$\mathcal{M}_{IG}^{\max}$	28.05	7.785e-03
$\mathcal{M}_{IG}^{\gamma}$	36.97	8.537e-03
$\mathcal{M}_{I}$	22.68	8.901e-02

Table 1: Test case 1: maximum aspect ratio and surface mismatch for different metrics.

	$\mathcal{M}_I$		$\mathcal{M}_{IG}^{\max}$		$\mathcal{M}_{IG}^{\gamma}$	
	isotropy	anisotropy	isotropy	anisotropy	isotropy	anisotropy
elements	2664	2618	3483	3434	2952	2925
e_{tot}	3.654e-03	1.195e-03	3.648e-03	9.160e-04	4.334e-03	1.392e-03
e_{mean}	1.371e-06	4.568e-07	1.047e-06	2.667e-07	1.468e-06	4.762e-07
$e_{\max}$	6.431e-05	3.135e-05	6.566e-05	1.669e-05	1.027e-04	5.424e-05

Table 2: Test case 1: anisotropy versus isotropy for a fixed cardinality of the mesh.

Then, we perform in some sense the dual check, i.e., we fix the accuracy (`TOL` in `MeshAdaptation`) and we assess the gain in terms of computational cost. The results are collected in Table 3. The dimension of the linear system we are led to solve in the anisotropic framework is remarkably lower. The maximum gain is yielded by the approach based on the maximum metric (one ninth of elements!) and, also in the worst case identified by metric $\mathcal{M}_I$, we reduce of one fifth the number of degrees of freedom.

A cross comparison between Tables 2 and 3 seems to suggest that the most strategical choice to exploit the computational advantages provided by an anisotropic mesh adaptation is represented by metric $\mathcal{M}_{IG}^{\max}$.

Convergence analysis We perform a twofold check in terms of convergence. First, we perform an asymptotic analysis of both the interpolation and the geometric error estimators. As shown in Figure 12, left the estimator η_I exhibits the theoretical expected trend as a function of the mesh cardinality $\#\mathcal{T}$, namely the rate of convergence turns out to be of the first order with respect to $1/\#\mathcal{T}$. Concerning the geometric error estimator, accordingly to [14], we expect a higher order of convergence. This statement is confirmed by the trend of η_G characterized by an order of about 1.5 with respect to $1/\#\mathcal{T}$. The different order of convergence of η_I and η_G justifies also in some respect the good performances of the adaptation procedure driven solely by the interpolation information, for a sufficiently fine mesh.

As a second check, we have verified how the selection of a specific metric to drive the adaptive algorithm may influence the order of convergence of the global

	$\mathcal{M}_I$		$\mathcal{M}_{IG}^{\max}$		$\mathcal{M}_{IG}^{\gamma}$	
	isotropy	anisotropy	isotropy	anisotropy	isotropy	anisotropy
elements	11479	2009	18201	2024	16548	2031
e_{tot}	3.168e-03	3.529e-03	3.159e-03	3.373e-03	3.049e-03	3.441e-03
e_{mean}	2.759e-07	1.756e-06	1.735e-07	1.666e-06	1.842e-07	1.694e-06
$e_{\max}$	6.557e-05	1.814e-04	6.619e-05	2.089e-04	7.004e-05	1.651e-04

Table 3: Test case 1: anisotropy versus isotropy for a fixed accuracy of the mesh.

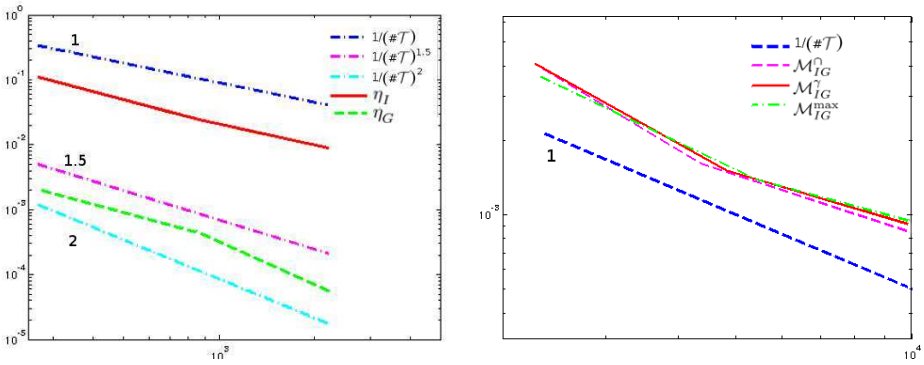

Figure 12: Test case 1: convergence history for the estimators η_I (solid line) and η_G (dashed line) in a loglog plot (left); convergence trend of the global error estimator when the adaptive procedure is driven by diverse metrics in a loglog plot (right).

error estimator η_{IG}. The numerical validation shows that no significant difference is detected by selecting a different metric and, for all the choices of $\mathcal{M}$, the order of convergence of the global error estimator is one. In Figure 12, right we provide an enlarged view of such a comparison, which shows the slight difference among the procedures associated with $\mathcal{M}_{IG}^{\cap}$, $\mathcal{M}_{IG}^{\max}$ and $\mathcal{M}_{IG}^{\gamma}$.

Robustness of the error estimators We investigate the robustness of the error estimators η_I and η_G, by computing the associated effectivity index

$$\text{E.I.}_I = \frac{\eta_I}{\|f - I_h f^E\|_{L^1(\Gamma)}}, \qquad \text{E.I.}_G = \frac{\eta_G}{\|d - I_h d\|_{L^1(\Gamma)}}, \tag{29}$$

respectively. Of course, the optimal value is 1 but, as usual, at least a stagnation of the value of the effectivity index is desirable, when the number of the mesh elements increases. Such a stagnation is mirrored by Table 4 for both the error estimators η_I and η_G, whose effectivity index settles around the value 1.4 and 0.8, respectively. Thus, while the interpolation error estimator slighly overestimates the actual error, an underestimation of the geometric error is provided by η_G.

elements	E.I.$_I$	E.I.$_G$
2920	1.6083	0.927002
6635	1.4692	0.888572
10573	1.4105	0.851926
14240	1.4798	0.874772

Table 4: Test case 1: effectivity index for the interpolation and the geometric errors.

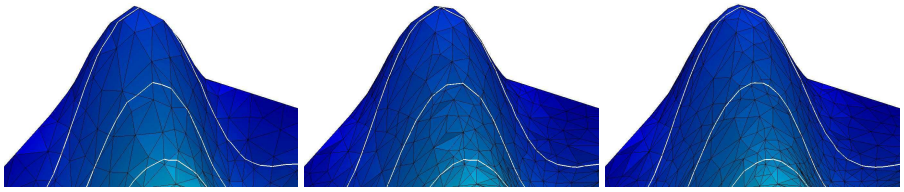

Figure 13: Test case 1: particular of the function f_1 on the surface Γ_1 for $\gamma = 0.1$ (left), 0.5 (middle), 0.7 (right).

Sensitivity with respect to γ We analyze the sensitivity of the adapted mesh yielded by the metric M^{γ}_{IG} with respect to the value of the parameter γ. To this aim, we fix the tolerance `TOL` to 2.e-05 and we choose $\gamma = 0.1, 0.5$ and 0.7. This choice leads to gradually increase the contribution of interpolation information in the metric M^{γ}_{IG}. Notice that the selected `TOL` is sufficiently small to ensure a rather accurate description of the surface independently of the value γ and in accordance with what stated in the first paragraph of this section. We focus on the peak at $(1, 1)$ since, at a glance, the difference among the whole adapted meshes is not so striking.

Figure 13 depicts the enlarged view of the adapted mesh for the three values of γ, together with the contour lines of the solution. We appreciate that the gradual inclusion of the interpolation information provides smoother contour lines, together with a slight increase of the mesh cardinality and of the aspect ratio of the elements which are correctly stretched to follow the directionalities of the surface.

Mismatch between Γ_h and $I_h d$ As last check we furnish a numerical support to the assumption made in the statement of Proposition 3. To verify that the zero level set of function $I_h d$ may be assumed as a surrogate of the discrete surface Γ_h, we compute the value of $I_h d$ on the adapted mesh Γ_h and we check if such a value approaches zero when the surface mesh is gradually adapted.

Figure 14 certifies the expected trend. We plot the interpolated distance function $I_h d$ on three adapted meshes consisting of 1643, 3792 and 6051 triangular faces (top-bottom), respectively. The values assumed by $I_h d$ exhibit a more uniform distribution and are closer to zero as the mesh is progressively adapted. More-

over, the maximum value reached by $I_h d$ also on the coarsest grid is not so large (about 8.e-03). This confirms that $I_h d$ may be reasonably employed to represent the discrete surface Γ_h.

5.2.2 Test case 2: a closed surface

Let Γ_2 be the toroidal surface coinciding with the zero level set of the signed distance function $d_2 : [-1.5, 1.5] \times [-1.5, 1.5] \times [-0.5, 0.5] \to \mathbb{R}$ such that

$$d_2(\mathbf{x}) = d_2(x_1, x_2, x_3) = \left(0.5 - \sqrt{x_1^2 + x_2^2}\right)^2 + x_3^2 - 1.$$

On this surface we assign the function $f_2 : \Gamma_2 \to \mathbb{R}$ given by

$$f_2(\mathbf{x}) = f_2(x_1, x_2, x_3) = 100 \tanh(40 x_1)$$

which essentially assumes the two constant values -100 and 100 separated by a steep gradient located in correspondence with the two unitary circumferences in the plane $x_2 O x_3$ and centered at (0, -1,0) and (0,1,0), respectively (see Figure 15 for the colorplot of the function).

On this new configuration we repeat some of the numerical controls performed in the first test case.
For this purpose, we run the adaptive algorithm `MeshAdaptation` by setting `TOL` = 5.e-03, `maxIter`= 10. Moreover, we fix $\gamma = 2/3$ for the parameter mixing the interpolation with the geometric information in the definition of $\mathcal{M}_{IG}^{\gamma}$.

Comparison among metrics We collect in Figure 16 the adapted meshes generated by exploiting the four metrics $\mathcal{M}_{IG}^{\cap}$, $\mathcal{M}_{IG}^{\max}$, $\mathcal{M}_{IG}^{\gamma}$ and $\mathcal{M}_I$, respectively. The layer is sharply captured by the four metrics via thin elements correctly oriented (see Figure 19). The coarsest grids are the ones predicted via $\mathcal{M}_{IG}^{\cap}$ (about 7600 triangles) and $\mathcal{M}_I$ (about 5100 triangles), whereas the other two meshes are constituted by a similar number of triangular faces, about equal to 9200.
Unlike test case 1, the limits of the adaptive procedure associated with the metric $\mathcal{M}_I$ are evident despite the many elements (i.e., the reduced tolerance). Indeed, the shape of Γ_2 is badly captured as highlighted by the very irregular areas on the surface in Figure 16 (d) and by the largest value of $d_{\max}$ in Table 5.
The intersection metric locates the anisotropic elements essentially in correspondence with the layer and correctly stretches them (see Figure 19 (a)). Nevertheless, analogously to the previous test case, the anisotropic features of the corresponding adapted mesh are less meaningful compared with the ones yielded by the other metrics. This is confirmed by the details in Figure 19 (b)-(c) as well as by the values of $\sigma_{\max}$ in Table 5, which, in general, highligth that the problem at hand is characterized by a more strongly anisotropic trend with respect to the case in § 5.2.1 (one order of magnitude distinguishes the values in Tables 5 and 1).

The details in Figure 17 and 18 on regions where f_2 is constant, corroborate on the one hand the fact that the absence of geometric information in $\mathcal{M}_I$ leads to

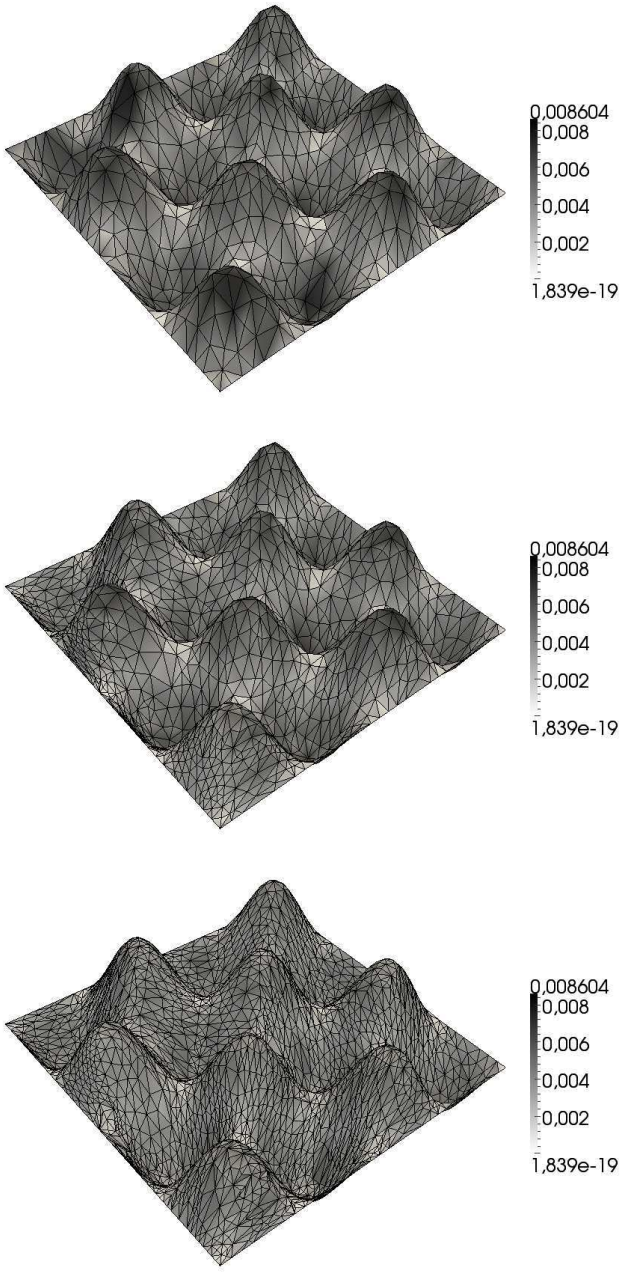

Figure 14: Test case 1: evaluation of the distance $I_h d$ on the adapted mesh Γ_h for an increasing number of mesh elements (top-bottom).

a very inaccurate approximation of Γ_2 (in such areas the interpolation information are not so meaningful while the geometric information is fully absent; see Fig-

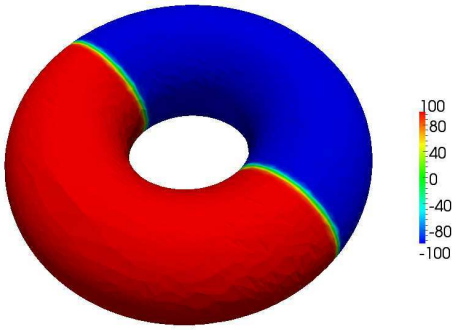

Figure 15: Function f_2 on the surface Γ_2.

metric	$\sigma_{\max}$	$d_{\max}$
$\mathcal{M}_{IG}^{\cap}$	9.967e+00	2.174e-02
$\mathcal{M}_{IG}^{\max}$	3.105e+01	2.359e-02
$\mathcal{M}_{IG}^{\gamma}$	2.601e+01	2.259e-02
$\mathcal{M}_{I}$	6.176e+01	1.168e-01

Table 5: Test case 2: maximum aspect ratio and surface mismatch for different metrics.

ure 17 (d) and 18 (d) and also the detail in Figure 19 (d)); on the other hand, the more isotropic nature of the mesh predicted by the metric $\mathcal{M}_{IG}^{\cap}$ is confirmed (see Figure 17 (a) and 18 (a)).

Anisotropy versus isotropy We verify the benefits led by an anisotropic mesh adaptation on an isotropic standard one via the values collected in Tables 6 and 7. As for the first test case, we exclude from this check the adaptive procedure driven by $\mathcal{M}_{IG}^{\cap}$, while computing the errors e_{tot}, e_{mean}, $e_{\max}$ in (27) for the other three metrics.

In Table 6, the comparison between anisotropy and isotropy is performed after fixing the number of elements. Both the total and the mean error reduce of a factor about equal to one half and the accuracy of the approximation improves also in terms of maximum error (this trend is not ensured in Table 2).
If viceversa, we fix the accuracy and we compare the two strategies in terms of number of elements as in Table 7, we get the expected reduction in the anisotropic case, with a factor of one third for $\mathcal{M}_I$ and $\mathcal{M}_{IG}^{\max}$ and of one half for $\mathcal{M}_{IG}^{\gamma}$.

A comparison across Tables 6 and 7 identifies $\mathcal{M}_I$ and $\mathcal{M}_{IG}^{\max}$ as the best choices from a computational viewpoint. Nevertheless, the remarks in the previous paragraph suggest the metric $\mathcal{M}_{IG}^{\max}$ as the one to be chosen.

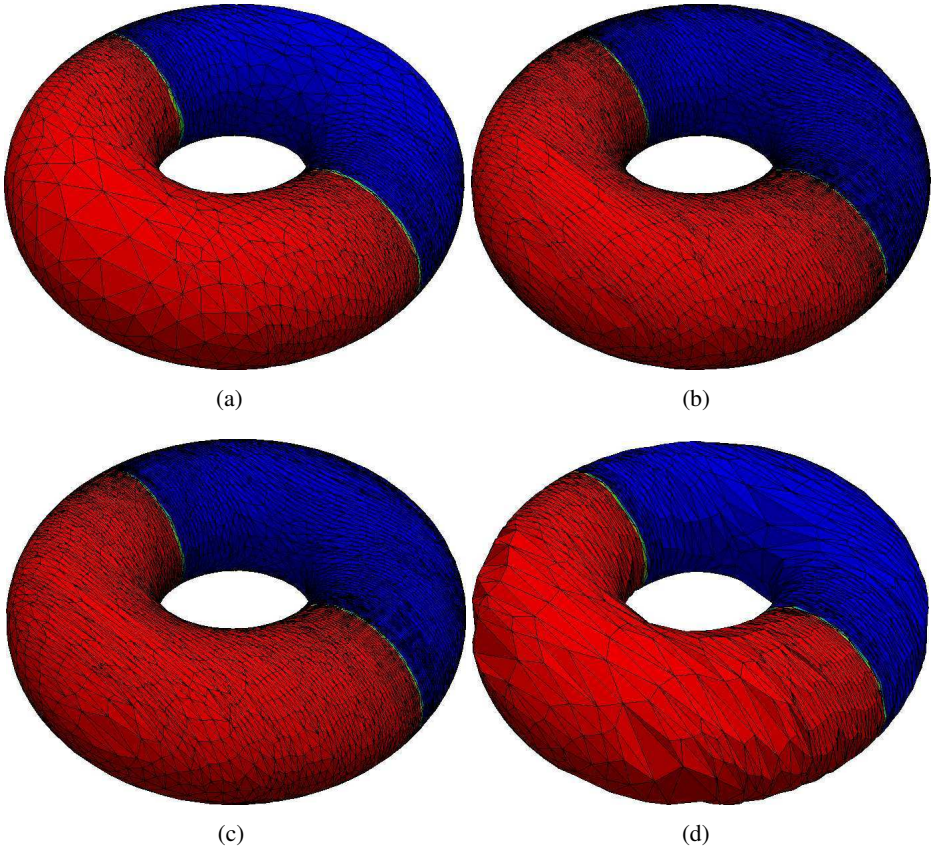

Figure 16: Test case 2: adapted mesh $\mathcal{T}_h^A$ generated via the metric (a) $\mathcal{M}_{IG}^{\cap}$, (b) $\mathcal{M}_{IG}^{\max}$, (c) $\mathcal{M}_{IG}^{\gamma}$ and (d) $\mathcal{M}_I$.

Convergence analysis We analyze the asymptotic trend of both the estimators η_I and η_G as a function of $\#\mathcal{T}_h$. Figure 20 (left) shows the associated loglog plot. The interpolation error estimator is characterized by an order of convergence equal to one with respect to $1/(\#\mathcal{T}_h)$, exactly as in Figure 12 (left). The geometric error estimator converges faster than η_I, with an order very close to two (instead of the order 1.5 in Figure 12 (left)).

Figure 20 (right) confirms the slight sensitivity of the rate of convergence of the global estimator with respect to the metric driving the adaptive procedure, by providing a zoom in, on the convergence history of η_{IG}. Indipendently of the selected metric, we confirm a convergence of the first order.

Robustness of the error estimators We compute the effectivity indices in (29) on four adapted meshes to check the robustness of the interpolation and the geometric error estimators. The corresponding values are gathered in Table 8. A sort of stagnation is detected for both the indices, we say around the values 1.7 and 0.6, respectively. This means that an overestimation of η_I and an underestimation of

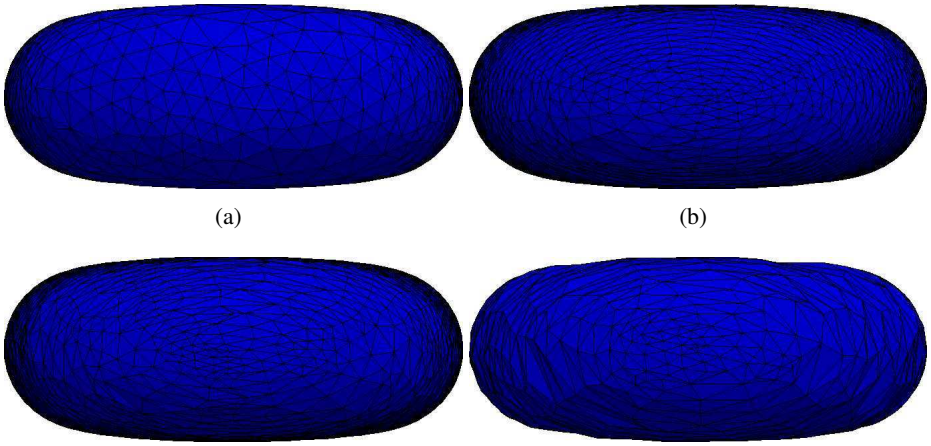

(a) (b) (c) (d)

Figure 17: Test case 2: detail on the constant part associated with the minimum value of f_2 for the mesh generated via the metric (a) $\mathcal{M}_{IG}^{\cap}$, (b) $\mathcal{M}_{IG}^{\max}$, (c) $\mathcal{M}_{IG}^{\gamma}$ and (d) $\mathcal{M}_I$.

	$\mathcal{M}_I$		$\mathcal{M}_{IG}^{\max}$		$\mathcal{M}_{IG}^{\gamma}$	
	isotropy	anisotropy	isotropy	anisotropy	isotropy	anisotropy
elements	3376	3640	3672	3652	1548	1660
e_{tot}	1.901e-01	8.884e-02	1.864e-01	8.887e-02	5.820e-01	3.463e-01
e_{mean}	5.633e-05	2.440e-05	5.078e-05	2.429e-05	3.759e-04	2.086e-04
$e_{\max}$	2.237e-03	1.646e-03	1.848e-02	1.641e-03	1.648e-02	8.074e-03

Table 6: Test case 2: anisotropy versus isotropy for a fixed cardinality of the mesh.

η_G take place, with a more accentuated trend in both the directions with respect to the first test case.

6 Conclusions and future developments

In this work we have proposed a new approach for an anisotropic control of the error related to the approximation of an $H^1(\Gamma)$-function via a piecewise linear quasi-interpolant operator on a surface $\Gamma \subset \mathbb{R}^3$ defined implicitly. The proposed analysis automatically takes into account the approximation of the function and the fitting of the surface, thus leading to a unique adaptive procedure able to contemporary match the directionalities of f and Γ.

The numerical validation in § 5.2 confirms the robustness of the adaptive tool. Both the numerical tests seem to identify the maximum metric $\mathcal{M}_{IG}^{\max}$ as the best performing one with a view to an anisotropic mesh adaptation. The expected advantages with respect to a standard isotropic mesh adaptation are verified on both

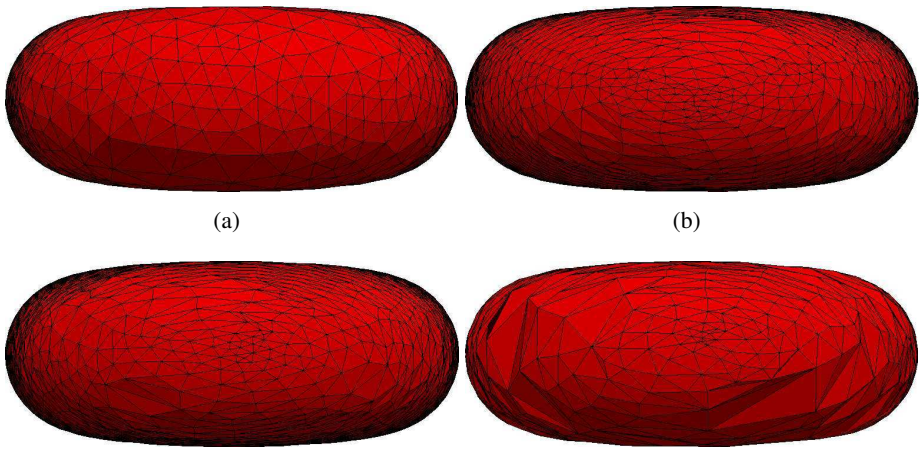

(a) (b) (c) (d)

Figure 18: Test case 2: detail on the constant part associated with the maximum value of f_2 for the mesh generated via the metric (a) $\mathcal{M}_{IG}^{\cap}$, (b) $\mathcal{M}_{IG}^{\max}$, (c) $\mathcal{M}_{IG}^{\gamma}$ and (d) $\mathcal{M}_I$.

	$\mathcal{M}_I$		$\mathcal{M}_{IG}^{\max}$		$\mathcal{M}_{IG}^{\gamma}$	
	isotropy	anisotropy	isotropy	anisotropy	isotropy	anisotropy
elements	11030	4732	11030	4746	8162	4084
e_{tot}	6.327e-02	6.490e-02	6.327e-02	6.420e-02	8.656e-02	8.733e-02
e_{mean}	5.736e-06	1.371e-05	5.736e-06	1.352e-05	1.060e-05	2.138e-05
$e_{\max}$	4.212e-04	1.019e-03	4.212e-04	1.019e-03	7.884e-04	1.775e-03

Table 7: Test case 2: anisotropy versus isotropy for a fixed accuracy of the mesh.

open and closed surfaces.
The convergence analysis corroborates the results expected from the theory, i.e., an order of convergence equal to one for the interpolation error and a higher order for the geometric contribution, indipendently of the selected global metric.
Concerning the robustness of the separate error estimators, the values of the corresponding effectivity index highlight a slight overestimation trend characterizing the interpolaton estimator whereas the geometric estimator underestimates the actual error.
Finally, a cross comparison between the two test cases shows that the anisotropic features predicted by the mesh adaptation procedure become more evident in the second and more challenging setting, while all the conclusions drawn above still hold.

The promising results of this work suggest us as a next step the development of a corresponding *a-posteriori* error analysis, possibly in a goal-oriented setting [3, 30, 40].

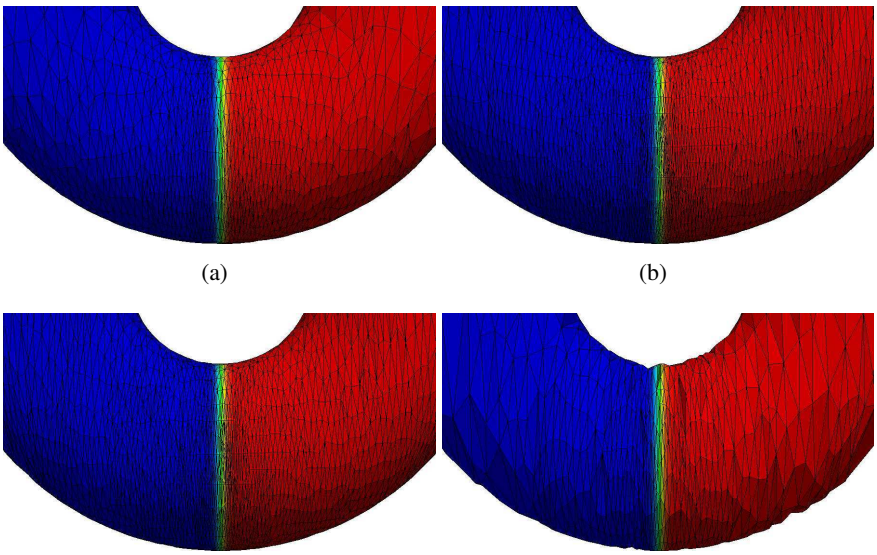

(a) (b) (c) (d)

Figure 19: Test case 2: detail in correspondence with the layer for the adapted mesh $\mathcal{T}_h^A$ generated via the metric (a) $\mathcal{M}_{IG}^{\cap}$, (b) $\mathcal{M}_{IG}^{\max}$, (c) $\mathcal{M}_{IG}^{\gamma}$ and (d) $\mathcal{M}_I$.

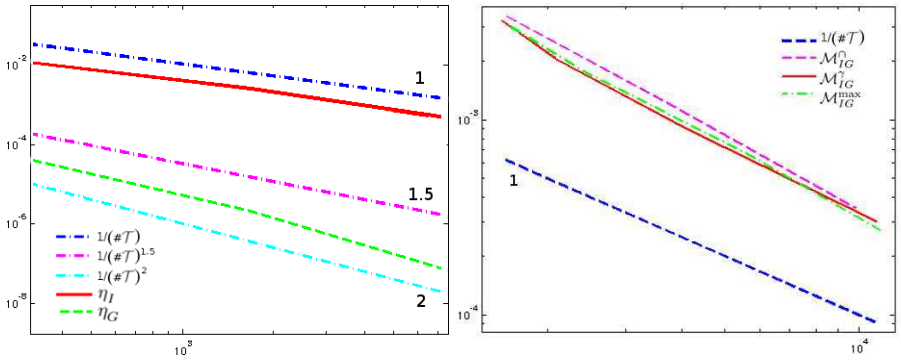

Figure 20: Test case 2: convergence history for the estimators η_I (solid line) and η_G (dashed line) in a loglog plot (left); convergence trend of the global error estimator when the adaptive procedure is driven by diverse metrics in a loglog plot (right).

Acknowledgment

The second author gratefully acknowledge the financial support of the Project MIUR–PRIN 2010/2011 “Innovative Methods for Water Resources under Hydro-Climatic Uncertainty Scenarios”.

elements	E.I.$_I$	E.I.$_G$
4152	1.7695	0.6102
11818	1.8502	0.6348
15506	1.6897	0.6854
22144	1.694	0.6401

Table 8: Test case 2: effectivity index for the interpolation and the geometric errors.

References

[1] T. APEL, *Anisotropic Finite Elements: Local Estimates and Applications*, Advances in Numerical Mathematics, Teubner, Stuttgart, 1999.

[2] T. APEL AND C. PESTER, *Clément-type interpolation on spherical domains - interpolation error estimates and application to a posteriori error estimation*, IMA J. Numer. Anal., 25 (2005), pp. 310–336.

[3] R. BECKER AND R. RANNACHER, *An optimal control approach to a posteriori error estimation in finite element methods*, Acta Numer., 10 (2001), pp. 1–102.

[4] A. BELME, A. DERVIEUX AND F. ALAUZET, *Time accurate anisotropic goal-oriented mesh adaptation for unsteady flows*, J. Comput. Phys., 231 (19) (2012), pp. 6323–6348.

[5] H. BOROUCHAKI, P. LAUG AND P.L. GEORGE, *Parametric surface meshing using a combined advancing-front generalized Delaunay approach*, Int. J. Numer. Meth. Engrg., 49 (2000), pp. 233–259.

[6] R. BOUSSETTA, T. COUPEZ AND L. FOURMENT, *Adaptive remeshing based on a posteriori error estimation for forging simulation*, Comput. Methods Appl. Mech. Engrg., 195 (48-49) (2006), pp. 6626–6645.

[7] M.J. CASTRO-DIAZ, F. HECHT, B. MOHAMMADI AND O. PIRONNEAU, *Anisotropic unstructured mesh adaptation for flow simulations*, Int. J. Numer. Meth. Fluids, 25 (4) (1997), pp. 475–491.

[8] PH. CIARLET, *The Finite Element Method for Elliptic Problems*, North-Holland Publishing Company, Amsterdam, 1978.

[9] PH. CLÉMENT, *Approximation by finite element functions using local regularization*, RAIRO Anal. Numer., 2 (1975), pp. 77–84.

[10] T. COUPEZ, *Metric construction by length distribution tensor and edge based error for anisotropic adaptive meshing*, J. Comput. Phys., 230 (7) (2011), pp. 2391–2405.

[11] F. DASSI, B. ETTINGER, S. PEROTTO AND L.M. SANGALLI, *A mesh simplification strategy for a spatial regression analysis over the cortical surface of the brain* MOX Report 31/2013, Dipartimento di Matematica, Politecnico di Milano (2013).

[12] A. DEDNER, P. MADHAVAN AND B. STINNER, *Analysis of the discontinuous Galerkin method for elliptic problems on surfaces*, IMA J. Numer. Anal., 33 (3) (2013), pp. 952–973.

[13] A. DEMLOW, *Higher-order finite element methods and pointwise error estimates for elliptic problems on surfaces*, SIAM J. Numer. Anal., 47 (2) (2009), pp. 805–827.

[14] A. DEMLOW AND G. DZIUK, *An adaptive finite element method for the Laplace-Beltrami operator on implicity defined surfaces*, SIAM J. Numer. Anal., 45 (2007), pp. 421–442.

[15] T.K. DEY, A.N. HIRANI, B. KRISHNAMOORTHY AND G. SMITH, *Edge contractions and simplicial homology*, CoRR, 2013.

[16] G. DZIUK, *Finite elements for the Beltrami operator on arbitrary surfaces*, Partial Differential Equation Calc. Var., 1357 (1988), pp. 142–155.

[17] G. DZIUK AND C.M. ELLIOTT, FINITE ELEMENT METHODS FOR SURFACE PDES, Acta Numer., 22 (2013), pp. 289–396.

[18] H. EDELSBRUNNER, *Geometry and Topology for Mesh Generation*, Cambridge University Press, 2001.

[19] P.E. FARRELL, S. MICHELETTI AND S. PEROTTO, *An anisotropic Zienkiewicz-Zhu type error estimator for 3D applications*, Int. J. Numer. Methods Engrg., 85 (2011), pp. 671–692.

[20] P.E. FARRELL, S. MICHELETTI AND S. PEROTTO, *A recovery-based error estimator for anisotropic mesh adaptation in CFD*, Bol. Soc. Esp. Mat. Apl., 50 (2011), pp.115–138.

[21] F. FIERRO AND A. VEESER, *A posteriori error estimators, gradient recovery by averaging, and superconvergence*, Numer. Math., 103 (2006), pp. 267–298.

[22] L. FORMAGGIA AND S. PEROTTO, *New anisotropic a priori error estimates*, Numer. Math., 89 (2001), pp. 641–667.

[23] L. FORMAGGIA AND S. PEROTTO, *Anisotropic error estimates for elliptic problems*, Numer. Math., 94 (2003), pp. 67–92.

[24] P.J. FREY AND H. BOROUCHAKI, *Geometric surface mesh optimization*, Comput. Visual. Sci., 1 (3) (1998), pp. 113–121.

[25] P.J. FREY AND H. BOROUCHAKI, *Surface meshing using a geometric error estimate*, Int. J. Numer. Meth. Engng., 50 (2003), pp. 227–245.

[26] M. GARLAND AND P.S. HECKBERT, *Surface simplification using quadric error metrics*, in: Proceedings of the 24th Annual Conference on Computer Graphics and Interactive Techniques, SIGGRAPH 97, ACM Press/Addison-Wesley Publishing Co., New York, USA, 1997.

[27] P.L. GEORGE AND H. BOROUCHAKI *Delaunay Triangulation and Meshing-Application to Finite Element*, Editions Hermes, Paris, 1998.

[28] E.H. GEORGOULIS, E. HALL AND P. HOUSTON, *Discontinuous Galerkin methods for advection-diffusion-reaction problems on anisotropically refined meshes*, SIAM J. Sci. Comput., 30 (1) (2007), pp. 246–271.

[29] D. GILBARG AND N.S. TRUDINGER *Elliptic Partial Differential Equations of Second Order*, Springer, Berlin 1998.

[30] M.B. GILES AND E. SÜLI,*Adjoint methods for PDEs: a posteriori error analysis and postprocessing by duality*, Acta Numer., 11 (2002), pp. 145–236.

[31] G.H. GOLUB AND C.F. VAN LOAN, *Matrix Computations*, Second ed., The Johns Hopkins University Press, Baltimore, MD, 1996.

[32] E. HARTMANN, *On the curvatures of curves and surfaces defined by normalforms*, Computer aided geometric design, 16 (1999), pp. 355–376.

[33] M. HOLST, *Adaptive numerical treatment of elliptic systems on manifolds*, Adv. Comput. Math., 15 (2001), pp. 139–191.

[34] H. HOPPE, T. DEROSE, T. DUCHAMP, J. MCDONALD AND W. STUETZLE, *Mesh optimization*, in: Proceedings of the 20th Annual Conference on Computer Graphics and Interactive Techniques, SIGGRAPH 93, ACM Press/Addison-Wesley Publishing Co., New York, USA, 1993.

[35] F.C. HUANG, B.Y. CHEN AND Y.Y. CHUANG, *Progressive deforming meshes based on deformation oriented decimation and dynamic connectivity updating*, in: Proceedings of the 2006 ACM SIGGRAPH/Eurographics symposium on Computer animation, SCA 06, Eurographics Association, 2006.

[36] C.L. LAWSON, *Software for C^1 surface interpolation*, In: Rice, J.R. (ed.) Math. Software III, 161–194. Academic Press, New York, NY (1977).

[37] S. MICHELETTI AND S. PEROTTO, *Output functional control for nonlinear equations driven by anisotropic mesh adaptation: the Navier-Stokes equations*, SIAM J. Sci. Comput., 30 (2008), pp. 2817–2854.

[38] S. MICHELETTI AND S. PEROTTO, *Reliability and efficiency of an anisotropic ZienkiewiczZhu error estimator*, Comput. Methods Appl. Mech. Engrg., 195 (2006), pp. 799–835.

[39] P. MORIN AND R. NOCHETTO, *AFEM for the Laplace-Beltrami operator on graphs: design and conditional contraction property*, Math. Comp., 80 (2011), pp. 625–648.

[40] J.T. ODEN AND S. PRUDHOMME, *Goaloriented estimation and adaptivity for the finite element method*, Comput. Math. Appl., 41 (2001), pp. 735–756.

[41] J. PELLERIN, B. LÉVY, G. CAUMON AND A. BOTELLA, *Automatic surface remeshing of 3d structural models at specified resolution: A method based on voronoi diagrams*, Computers & Geosciences, 62 (2014), pp. 103–116.

[42] J. PERAIRE, M. VAHADATI, K. MORGAN AND O.C. ZIENKIEWICZ, *Adaptive remeshing for compressible flow computations*, J. Comput. Phys., 72 (1987), pp. 449–466.

[43] P.W. POWER, C.C. PAIN, M.D. PIGGOTT, F. FANG, G.J. GORMAN, A.P. UMPLEBY, A.J.H. GODDARD AND I.M. NAVON, *Adjoint a posteriori error measures for anisotropic mesh optimisation*, Comput. Math. Appl., 52 (8-9) (2006), pp. 1213–1242.

[44] R. RONFARD AND J. ROSSIGNAC, *Full-range approximation of triangulated polyhedra*, Computer Graphics Forum, 15 (3) (1996), pp. 67–76.

[45] E. SAUVAGE, J. F. REMACLE AND E. MARCHANDISE, *Metric field construction for anisotropic mesh adaptation with application to blood flow simulations*, Int. J. Numer. Meth. Biomed. Engng., 30 (2014), pp. 1326–1346.

[46] L.R. SCOTT AND S. ZHANG, *Finite element interpolation of non-smooth functions satisfying boundary conditions*, Math. Comp., 54 (1990), pp. 483–493.

[47] D.A. VENDITTI AND D.L. DARMOFAL, *Anisotropic grid adaptation for functional outputs: application to two-dimensional viscous flows*, J. Comput. Phys., 187 (2003), pp. 22–46.

[48] R. VERFÜRTH, *A Review of a Posteriori Error Estimation and Adaptive Mesh-Refinement Techniques*, WileyTeubner, New York, 1996.

MOX Technical Reports, last issues

Dipartimento di Matematica "F. Brioschi",
Politecnico di Milano, Via Bonardi 9 - 20133 Milano (Italy)

50/2014 Bartezzaghi, A.; Cremonesi, M.; Parolini, N.; Perego, U.
An explicit dynamics GPU structural solver for thin shell finite elements

51/2014 Dassi, F.; Perotto, S.; Formaggia, L.
A priori anisotropic mesh adaptation on implicitly defined surfaces

49/2014 D. Bonomi, C. Vergara, E. Faggiano, M. Stevanella, C. Conti, A. Redaelli, G. Puppini et al
Influence of the aortic valve leaflets on the fluid-dynamics in aorta in presence of a normally functioning bicuspid valve

48/2014 Penta, R; Ambrosi, D; Shipley, R.
Effective governing equations for poroelastic growing media

47/2014 Penta, R; Ambrosi, D; Quarteroni, A.
Multiscale homogenization for fluid and drug transport in vascularized malignant tissues

46/2014 Penta, R; Ambrosi, D.
The role of the microvascular tortuosity in tumor transport phenomena

45/2014 Pezzuto, S.; Ambrosi,D.; Quarteroni, A.
An orthotropic active-strain model for the myocardium mechanics and its numerical approximation

44/2014 Pezzuto, S.; Ambrosi,D.
Active contraction of the cardiac ventricle and distortion of the microstructural architecture

43/2014 Brugiapaglia, S.; Micheletti, S.; Perotto, S.
Compressed solving: a numerical approximation technique for PDEs based on compressed sensing

42/2014 Canale, A.; Vantini, S.
Constrained Functional Time Series: an Application to Demand and Supply Curves in the Italian Natural Gas Balancing Platform